The McDonald Accelerating Stars Survey: Architecture of the Ancient Five-planet Host System Kepler-444

Zhoujian Zhang (张周健)[1,2,9] , Brendan P. Bowler[2] , Trent J. Dupuy[3] , Timothy D. Brandt[4] , G. Mirek Brandt[4] ,
William D. Cochran[5] , Michael Endl[6] , Phillip J. MacQueen[6] , Kaitlin M. Kratter[7] , Howard T. Isaacson[8] ,
Kyle Franson[2,10] , Adam L. Kraus[2] , Caroline V. Morley[2] , and Yifan Zhou[2,11]

[1] Department of Astronomy & Astrophysics, University of California, Santa Cruz, 1156 High St., Santa Cruz, CA 95064, USA
[2] Department of Astronomy, The University of Texas at Austin, Austin, TX 78712, USA
[3] Institute for Astronomy, University of Edinburgh, Royal Observatory, Blackford Hill, Edinburgh, EH9 3HJ, UK
[4] Department of Physics, University of California, Santa Barbara, Santa Barbara, CA 93106, USA
[5] Center for Planetary Systems Habitability and McDonald Observatory, The University of Texas at Austin, Austin, TX 78712, USA
[6] McDonald Observatory and the Department of Astronomy, The University of Texas at Austin, Austin, TX 78712, USA
[7] Department of Astronomy, University of Arizona, Tucson, AZ 85721, USA
[8] Department of Astronomy, University of California, Berkeley, 501 Campbell Hall #3411, Berkeley, CA 94720, USA

Abstract

We present the latest and most precise characterization of the architecture for the ancient ($\approx$11 Gyr) Kepler-444 system, which is composed of a K0 primary star (Kepler-444 A) hosting five transiting planets and a tight M-type spectroscopic binary (Kepler-444 BC) with an A–BC projected separation of 66 au. We have measured the system's relative astrometry using the adaptive optics imaging from Keck/NIRC2 and Kepler-444 A's radial velocities from the Hobby-Eberly Telescope and reanalyzed relative radial velocities between BC and A from Keck/HIRES. We also include the Hipparcos-Gaia astrometric acceleration and all published astrometry and radial velocities in an updated orbit analysis of BC's barycenter. These data greatly extend the time baseline of the monitoring and lead to significant updates to BC's barycentric orbit compared to previous work, including a larger semimajor axis ($a = 52.2^{+3.3}_{-2.7}$ au), a smaller eccentricity ($e = 0.55 \pm 0.05$), and a more precise inclination ($i = 85^{\circ}.4^{+0.3}_{-0.4}$). We have also derived the first dynamical masses of B and C components. Our results suggest that Kepler-444 A's protoplanetary disk was likely truncated by BC to a radius of $\approx$8 au, which resolves the previously noticed tension between Kepler-444 A's disk mass and planet masses. Kepler-444 BC's barycentric orbit is likely aligned with those of A's five planets, which might be primordial or a consequence of dynamical evolution. The Kepler-444 system demonstrates that compact multiplanet systems residing in hierarchical stellar triples can form at early epochs of the universe and survive their secular evolution throughout cosmic time.

Unified Astronomy Thesaurus concepts: Binary stars (154); Planetary system formation (1257); Astrometry (80)

1. Introduction

Stellar multiple systems are ubiquitous products of the star formation processes (e.g., Duquennoy & Mayor 1991; Fischer & Marcy 1992; Raghavan et al. 2010; Duchene & Kraus 2013; Offner et al. 2022). Thus, a substantial fraction of exoplanets might form in dynamical environments sculpted by stellar multiplicity, with distinct formation histories and orbital architectures from those with single stellar hosts. Close stellar binaries (with the semimajor axes, a, below a few au) can possess circumbinary protoplanetary disks massive enough to form P-type planets orbiting both stars (e.g., Doyle et al. 2011; Czekala et al. 2019), while wide-separation binaries (with a above a few tens of au) can host S-type planets orbiting either the primary or the secondary star (e.g., Hatzes et al. 2003; Campante et al. 2015).

The binarity of planet-hosting stars is expected to suppress planet formation, as stellar binaries can truncate the protoplanetary disk of either component (e.g., Artymowicz & Lubow 1994; Lubow et al. 2015; Miranda & Lai 2015), trigger disk turbulence and dynamically excite planetesimals' eccentricities and velocities (e.g., Thébault et al. 2006; Rafikov & Silsbee 2015; Silsbee & Rafikov 2015), and induce secular oscillations in planets' orbital inclinations and eccentricities via the Kozai–Lidov mechanism (e.g., Kozai 1962; Lidov 1962; Naoz et al. 2013). Indeed, observational studies have shown that the occurrence rate of exoplanets in stellar binaries tends to be smaller than those of wider binaries or single stars (e.g., Wang et al. 2014; Kraus et al. 2016; Moe & Kratter 2021; Ziegler et al. 2021). Moreover, the orbits of planet-hosting stellar binaries appear to be statistically aligned with those of the planets, while orbital inclinations of binaries without planets are likely isotropic (e.g., Behmard et al. 2022; Christian et al. 2022; Dupuy et al. 2022). The orbital alignment between binaries and planets could be primordial if both stellar components and the planets all form within the same massive disk or hierarchical cloud fragmentation that preserves orbital angular momenta (e.g., Sigalotti et al. 2018; Tokovinin 2018; Christian et al. 2022). Alternatively, for stellar binary systems formed in misaligned orbits with the protoplanetary disk, the presence of a wide stellar companion can torque the gaseous

disk into alignment by inducing disk precession and subsequent energy dissipation (e.g., Bate et al. 2000; Batygin 2012; Zanazzi & Lai 2018; Christian et al. 2022).

As a hierarchical triple-planet host system, Kepler-444 (Campante et al. 2015) provides an excellent laboratory for studying the impact of stellar multiplicity on the formation and dynamical evolution of planetary systems. Located at a distance of 36.52 ± 0.02 pc (Bailer-Jones et al. 2021), this system is composed of a K0 dwarf (Kepler-444 A) and a tight ($\lesssim 0.3$ au; Dupuy et al. 2016) M-type spectroscopic binary (Kepler-444 BC) with a projected separation of $1''8$ (or ≈ 66 au) from A. Kepler-444 A hosts a compact planetary system ($a = 0.04$–0.08 au) of five transiting planets with sub-Earth sizes ($R_p = 0.4$–0.7 $R_\oplus$) and mildly eccentric orbits ($e = 0.1$–0.3; Campante et al. 2015; Buldgen et al. 2019). Orbital periods of these planets (3–10 days) are close to, though not exactly matching, mean-motion resonances (Campante et al. 2015). Due to their proximity to the 5:4 resonance, planets Kepler-444 d and e induce significant transit timing variations in Kepler light curves, leading to measured photodynamical masses of $0.036^{+0.065}_{-0.020}$ $M_\oplus$ for planet d and $0.034^{+0.059}_{-0.019}$ $M_\oplus$ for planet e (Mills & Fabrycky 2017). These two planets thus have low densities, suggestive of water-rich or pure-silicate compositions.

One of the most astounding properties of this complex planetary system is its very old age of ≈ 11 Gyr, as supported by asteroseismology (e.g., Campante et al. 2015; Buldgen et al. 2019), stellar isochrones (e.g., Brewer et al. 2016; Johnson et al. 2017), a long stellar rotation period (e.g., Mazeh et al. 2015; Hall et al. 2021), and the system's Galactic thick-disk membership (e.g., Campante et al. 2015). Kepler-444 A is metal-poor ([Fe/H] $= -0.52 \pm 0.12$ dex) with enhanced α-abundance (Mack et al. 2018), consistent with the observed trends that compact multiplanet systems are more prevalent around metal-poor stars than metal-rich stars (e.g., Brewer et al. 2018) and that metal-poor stars with planets tend to have higher [α/Fe] than those without planets (e.g., Adibekyan et al. 2012). Kepler-444 also belongs to the Arcturus stellar stream (Arifyanto & Fuchs 2006), which likely has an extragalactic origin (e.g., Bovy et al. 2009; Bensby et al. 2014).

Constraining the barycentric orbit of Kepler-444 BC relative to A provides boundary conditions on the size and mass of the protoplanetary disk that resided around A, informs past and future dynamical interactions between the BC binary and the inner planets, and places this system in the context of statistical studies of planet-hosting stellar binaries (e.g., Behmard et al. 2022; Christian et al. 2022; Dupuy et al. 2022). Dupuy et al. (2016) provided the first constraints of Kepler-444 BC's barycentric orbit by combining A's multiepoch radial velocities (RVs), the relative RV between the BC and A components, and relative astrometry from 3 yr of monitoring using adaptive optics (AO) imaging. They found that BC has a highly eccentric orbit ($e \approx 0.86$), leading to a small A–BC separation of ≈ 5 au at periastron. This implies that the protoplanetary disk of Kepler-444 A was truncated and severely depleted of planet-forming solid material.

We have acquired new observations of Kepler-444 as part of the McDonald Accelerating Stars Survey (Bowler et al. 2021a, 2021b), an AO imaging program targeting stars with long-term RV trends and astrometric accelerations from Hipparcos and Gaia, which supplement the published astrometric and RV data used in Dupuy et al. (2016). Our new

relative astrometry of this system extends the time baseline of monitoring to 9 yr, and our new RVs bridge the epochs of two published data sets, spanning a total of 12 yr. The arrival of high-precision Gaia astrometry (Gaia Collaboration et al. 2016), when combined with Hipparcos, further informs the orbit analysis by providing the sky-projected astrometric acceleration (e.g., Brandt 2018, 2021; Fontanive et al. 2019; Currie et al. 2020; Bowler et al. 2021a, 2021b; Li et al. 2021; Bonavita et al. 2022; Franson et al. 2022; Kuzuhara et al. 2022), which complements the line-of-sight acceleration revealed by the primary star's RVs.

Here we combine our new observations and all published relative astrometry, absolute astrometry, and RVs of Kepler-444 to provide the latest constraints on the orbital architecture of this system. Our orbit analysis also sheds new insight into the properties of Kepler-444's protoplanetary disk. We describe our new observations of Kepler-444 in Section 2 and the extracted astrometry and RVs in Section 3. We then present the orbit analysis in Section 4 and discuss their physical implications in Section 5, followed by a brief summary in Section 6.

2. Observations

2.1. Adaptive Optics Imaging

We acquired natural guide star AO images of Kepler-444 on 2019 July 7 UT and 2022 July 12 UT with Keck/NIRC2 in its narrow field of view configuration (Wizinowich 2013). On 2019 July 7 UT, we took 10 frames in J band, with an integration of 0.053 s per coadd and 50 coadds per exposure. On 2022 July 12 UT, we took 10 frames in H band and 9 frames in K_S band with 0.018 s per coadd and 0.053 s per coadd, respectively (both with 100 coadds per exposure). Kepler-444 A and Kepler-444 BC are widely separated (by $1''8$) in our images, and the BC pair is unresolved, as seen from earlier-epoch NIRC2 data (e.g., Dupuy et al. 2016), suggesting a tight B–C separation of $\lesssim 0.3$ au (i.e., 1 pixel). In J-band images, Kepler-444 A is offset by ~ 500 mas from a round, partly transparent coronagraph mask with a radius of 300 mas (Figure 1). In other words, the closest separation between Kepler-444 A and this mask's edge (i.e., 200 mas) is more than 6 times wider than the circular radius (30 mas) adopted to measure A's centroid (see Section 3.1). Given that components of the Kepler-444 system are all outside the coronagraph mask, their relative astrometry should not be impacted by including this mask in the optical path for our J-band images, as suggested by Konopacky et al. (2016). Dome flats and dark frames were taken on the same night as each science data set.

We also download all previously published NIRC2 data of Kepler-444 (by Campante et al. 2015; Dupuy et al. 2016, 2022) from the Keck Observatory Archive.[12] These data were all taken in pupil-tracking mode and were observed on 2013 August 7 UT (PI: Kraus), 2014 July 28 UT (PI: Kraus), 2014 August 9 UT (PI: Barclay), 2014 November 30 UT (PI: Kraus), 2015 April 11 UT (PI: Liu), 2015 June 22 UT (PI: Mann), 2015 July 21 UT (PI: Kraus), and 2016 June 16 UT (PI: Ireland). We uniformly re-reduce all these published data along with our new observations to avoid any systematics in the relative astrometry caused by different reduction pipelines used in the literature and our work (Section 3).

---

[12] https://koa.ipac.caltech.edu/cgi-bin/KOA/nph-KOAlogin
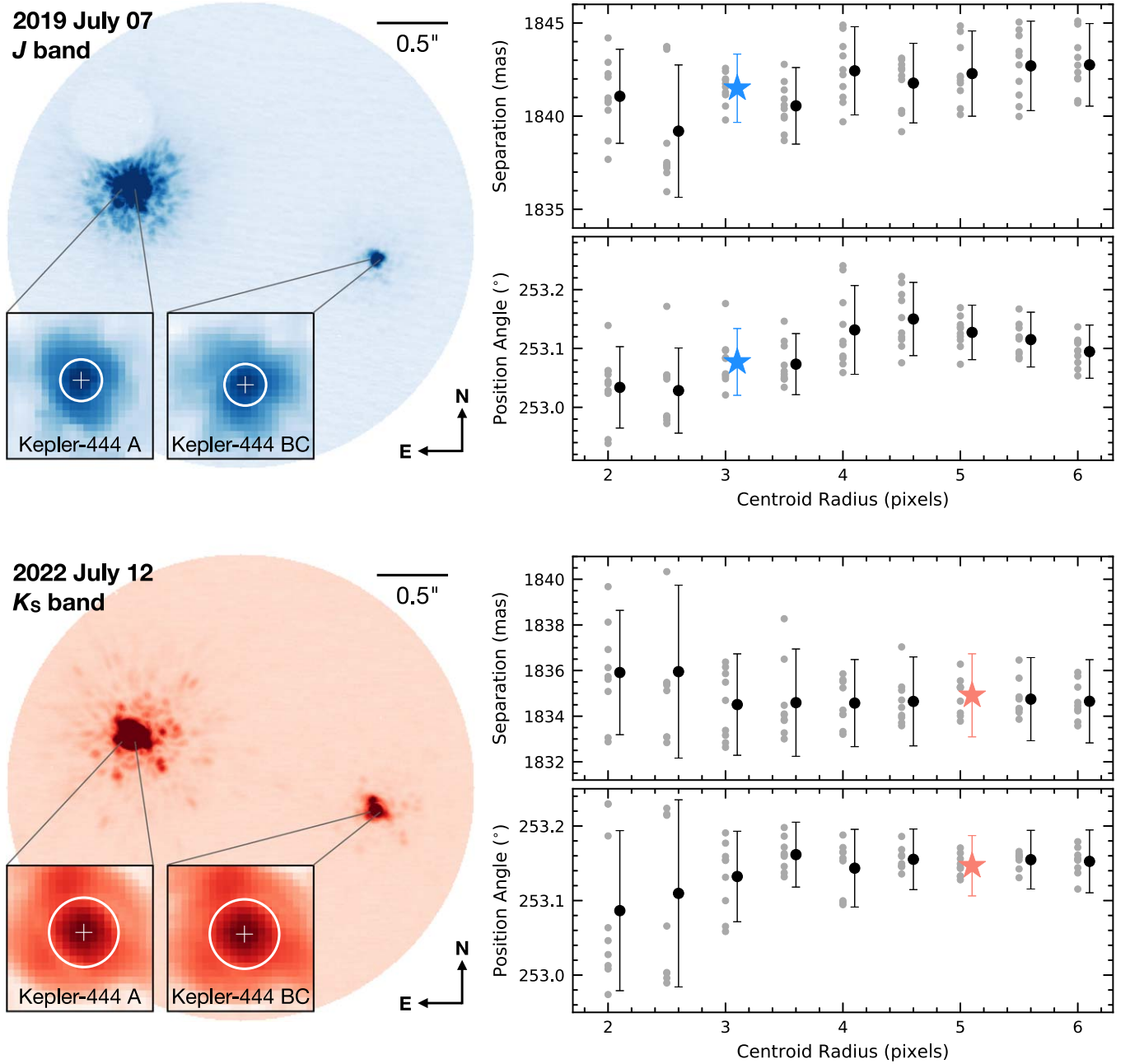
Figure 1. Top left: a typical reduced and north-aligned *J*-band science frame of Kepler-444 observed on 2019 July 7 UT. Insets present the 20 pixel × 20 pixel vicinity of A (left) and BC (right) components with their centroids marked by plus signs, computed using a 3-pixel-radius circular region (white circle). A coronagraph mask is visible to the northeast of Kepler-444 A and does not impact our relative astrometry measurements. Top right: centroids of A and BC iteratively computed using a range of circular radii (Section 3.1). At each radius, we show the computed separation and position angle of individual science frames observed on 2019 July 7 UT (gray circle), as well as the resulting separation and position angle measurements with uncertainties computed from Equation (2) (black circle). Our final separation and position angle measurements for the *J*-band data are based on a circular radius of 3 pixels and are highlighted as blue stars. Bottom: analysis of K_S-band data observed on 2022 July 12 UT with the same format as the top panel. The white circles in the insets and our final relative astrometry all correspond to a radius of 5 pixels.

2.2. Radial Velocities

We obtained precise RV measurements of Kepler-444 A using the High Resolution Spectrograph (HRS; Tull 1998) of the Hobby-Eberly Telescope (HET). We used the 316g5936 HRS configuration with a 2″-diameter optical fiber to obtain a spectral resolving power of $R \approx 60{,}000$. Twenty visits to the target were obtained in queue scheduled mode (Shetrone et al. 2007) between 2008 November 9 and 2013 July 1 UT, along with an I_2 gas absorption cell that provided the high-precision RV metric. A single spectrum of Kepler-444 A without the I_2

cell was obtained on 2008 September 30 UT to serve as the stellar spectral template. All HET/HRS spectra were reduced using an automated IRAF script that performs bias subtraction, scattered light removal, and flat-fielding. We also traced the aperture for each echelon spectral order for one-dimensional spectra extraction and calibrated the wavelength solution from the nightly Th–Ar hollow-cathode lamp spectra. Given that HET/HRS did not contain an exposure meter, we estimated the mid-exposure time to be the average of the exposure start and end time. We compute relative RVs of Kepler-444 A from the

Table 1
HET/HRS Relative Radial Velocities

Epoch (BJD)	RV_A (m s^{-1})	σ_{RV_A} (m s^{-1})
2,454,779.57424	34.21	3.44
2,455,020.91240	21.69	4.93
2,455,022.91033	25.32	4.54
2,455,049.83642	5.39	5.56
2,455,139.58038	8.80	3.41
2,455,292.93468	0.62	4.26
2,455,322.85609	2.78	4.12
2,455,525.55168	6.78	4.26
2,455,628.99753	4.46	5.38
2,455,686.84674	−12.13	4.86
2,455,730.74825	−0.39	4.92
2,455,837.66975	−1.40	3.52
2,455,869.57189	−13.94	3.61
2,456,127.66590	−7.60	5.72
2,456,194.68123	−1.69	3.97
2,456,202.66150	−8.00	3.68
2,456,208.64940	−17.84	3.23
2,456,224.60794	−14.73	3.51
2,456,363.99758	−21.12	4.46
2,456,474.95592	−11.12	5.98

observed spectra using the auSTRAL code (Endl et al. 2000) and list them in Table 1.

3. Astrometry and Radial Velocity Analysis

3.1. Relative Astrometry

We (re-)reduce new and published Keck/NIRC2 AO images (Section 2.1) in a uniform manner following standard procedures, including applying nonlinearity and bad pixel corrections, bias subtraction, flat-fielding, and cosmic-ray rejection. The geometric distortions are corrected using the Yelda et al. (2010) solution for data observed before the NIRC2 realignment on 2015 April 13 UT and the Service et al. (2016) solution for the more recent data sets. We measure the angular separation and position angle of Kepler-444 BC relative to A based on their centroids. For each system component in each distortion-corrected science frame, we first identify the highest-flux pixel and compute a flux-weighted centroid using all data within a certain radius of this brightest pixel. We then iterate this process by updating the circle center to the newly computed centroid position until the relative change in the centroid is below 10^{-6}. This calculation is carried out for a range of circular radii from 2 to 6 pixels (with intervals of 0.5 pixels), and the final relative astrometry is determined using a radius of 3 pixels (30 mas on the sky) in J band, 4 pixels (40 mas on the sky) in H band, and 5 pixels (50 mas on the sky) in $K'/K_{\rm cont}/K_S$ bands, as these values correspond to Keck's diffraction limit (Figure 1).

To evaluate systematic uncertainties of our inferred centroids, we simulate a point-spread function (PSF) centered at a random pixel location (fractional pixel locations are allowed) on a detector and then measure its centroid. The PSF is simply described by $I(u) = [2J_1(u)/u]^2$ with $u = \pi\lambda\theta/D$, where θ is the angular separation (in units of radians) of a given point on the detector from the PSF center, J_1 is the Bessel function of its first kind, $D = 10$ m is the aperture diameter of Keck, and λ is the effective wavelength of a given NIRC2 filter: 1.2434 μm for J band, 1.6197 μm for H band, 2.1084 μm for K' band, 2.2874 μm for $K_{\rm cont}$ band, and 2.1354 for K_S band. We sample the PSF into the

pixelated image with two versions of the plate scale as 9.952 mas pixel^{-1} (Yelda et al. 2010) and 9.971 mas pixel^{-1} (Service et al. 2016), corresponding to the detector properties before and after the NIRC2 realignment, respectively. Generating PSFs at random detector locations, we find that the differences between the measured and input centroid positions are all below 0.2 mas with a given combination of the band and plate scale. This systematic error is more than 5× smaller than the position uncertainty caused by the distortion correction (see below) and is thus ignored in the error budget of our measured relative astrometry.

Given the centroids of BC ($x_{i,\rm BC}$, $y_{i,\rm BC}$) and A ($x_{i,\rm A}$, $y_{i,\rm A}$) in each science frame (denoted by i), the on-detector separation (r_i; in units of pixels) and position angle (p_i; in units of degrees) are calculated as

$$r_i = [(x_{i,\rm BC} - x_{i,\rm A})^2 + (y_{i,\rm BC} - y_{i,\rm A})^2]^{1/2}$$

$$p_i = \text{mod}\left[-2 \times \arctan\left(\frac{x_{i,\rm BC} - x_{i,\rm A}}{r_i + y_{i,\rm BC} - y_{i,\rm A}}\right)\right.$$
$$\left. \times 180°/\pi, 360°\right]. \tag{1}$$

Here p_i becomes 180° when $x_{i,\rm BC} - x_{i,\rm A} = 0$ and $y_{i,\rm BC} - y_{i,\rm A} < 0$. At a given epoch, we compute these parameters' mean and standard deviation ($\bar{r}$, σ_r; $\bar{p}$, σ_p) over all science frames and convert them into an on-sky separation (ρ; in units of mas) and position angle (θ; in units of degrees) as (also see Section 4.3 of Bowler et al. 2018)

$$\rho = s\bar{r}$$
$$\sigma_\rho = \rho[(\sigma_s/s)^2 + (\sigma_r/\bar{r})^2 + 2(\sigma_{d,r}/\bar{r})^2]^{1/2}$$
$$\theta = \bar{p} + \text{PARANG} + \text{ROTPOSN} - \text{INSTANGL} - \theta_{\rm north}$$
$$\sigma_\theta = [\sigma_p^2 + \sigma_{\theta,\rm north}^2 + (s\sigma_{d,r}/\rho \times 180°/\pi)^2]^{1/2}. \tag{2}$$

For data taken before (and after) the NIRC2 realignment, we adopt a plate scale s and uncertainty σ_s as 9.952 ± 0.002 mas pixel^{-1} (9.971 ± 0.004 mas pixel^{-1}) and the north orientation offset $\theta_{\rm north}$ and its uncertainty $\sigma_{\theta,\rm north}$ as $0°.252 \pm 0°.009$ ($0°.262 \pm 0°.020$) (Yelda et al. 2010; Service et al. 2016). Here $\sigma_{d,r} = 0.1$ pixels, representing the typical pixel position uncertainty near each component's centroid due to the distortion correction. We extract values of PARANG (parallactic angle), ROTPOSN (rotator user position), and INSTANGL (zero-point of the NIRC2 position angle) from FITS headers of our data. The uniformly measured relative astrometry is summarized in Table 2.

Our latest-epoch AO images reveal that the separation and position angle of BC's barycenter relative to A is significantly decreasing and increasing with time, respectively, due to the orbital motion. These trends were not well constrained based on the astrometric monitoring prior to the year 2017 (e.g., Dupuy et al. 2016, 2022).

3.2. Absolute Astrometry

While Kepler-444 BC was not detected by Hipparcos or Gaia DR1 at the time of the previous analysis (Dupuy et al. 2016), both A and BC now have Gaia EDR3 proper motions of ($\mu_\alpha \cos\delta$, μ_δ) = (94.64 ± 0.02, −632.27 ± 0.02) mas yr^{-1} and (94.51 ± 0.05, −630.78 ± 0.08) mas yr^{-1}, respectively (Gaia Collaboration et al. 2016, 2021), which is particularly useful for

Table 2
Relative Astrometry of Kepler-444

Date (UT)	Epoch (yr)	Filter	Data References	Separation (mas)	Position Angle (deg)
2013 Aug 7	2013.598	K'	Dupuy et al. (2016)	1842.57 ± 1.48	252.911 ± 0.046
2014 Jul 28	2014.571	K_{cont}	Dupuy et al. (2016)	1843.55 ± 1.69	252.876 ± 0.039
2014 Aug 9	2014.604	K'	Campante et al. (2015)	1841.67 ± 1.62	252.743 ± 0.037
2014 Nov 30	2014.913	K_{cont}	Dupuy et al. (2016)	1840.59 ± 1.61	252.743 ± 0.036
2015 Apr 11[a]	2015.276	K_{cont}	Dupuy et al. (2016)	1840.33 ± 2.55	252.760 ± 0.048
2015 Apr 11[a]	2015.276	K_{cont}	Dupuy et al. (2016)	1841.41 ± 1.55	252.764 ± 0.034
2015 Jun 22	2015.473	K_{cont}	Dupuy et al. (2022)	1842.39 ± 1.75	252.785 ± 0.039
2015 Jul 21	2015.552	K_{cont}	Dupuy et al. (2022)	1841.92 ± 1.76	252.783 ± 0.039
2016 Jun 16	2016.458	K_{cont}	Dupuy et al. (2022)	1840.78 ± 1.72	252.775 ± 0.047
2019 Jul 7	2019.514	J	This Work	1841.50 ± 1.83	253.077 ± 0.057
2022 Jul 12	2022.527	H	This Work	1835.78 ± 1.76	253.137 ± 0.045
2022 Jul 12	2022.527	K_S	This Work	1834.91 ± 1.82	253.147 ± 0.040

Note.
[a] We distinguish two sets of NIRC2 data taken with different detector sizes and rotator positions following Dupuy et al. (2016).

constraining the BC-to-A mass ratio (e.g., Brandt et al. 2021). In addition, Kepler-444 A exhibits a significant difference between its Gaia and the joint Hipparcos−Gaia long-term proper motions (reduced $\chi_\nu^2 = 1052$ for a constant proper-motion model; Brandt 2021), equivalent to an astrometric acceleration of $20.8 \pm 0.5 \, \mathrm{m \, s^{-1} \, yr^{-1}}$.

3.3. RV Acceleration of Kepler-444 A

Our HET/HRS RVs of Kepler-444 A show a significant linear trend of $-9.5 \pm 0.7 \, \mathrm{m \, s^{-1} \, yr^{-1}}$ with an rms of $7.0 \, \mathrm{m \, s^{-1}}$ (Figure 2). We also collect published RVs of Kepler-444 A from Keck/HIRES, including 163 epochs of RVs measured after the HIRES CCD upgrade on 2004 August 18 UT (Sozzetti et al. 2009; Dupuy et al. 2016; Butler et al. 2017) and 4 epochs before the upgrade (Sozzetti et al. 2009). We treat these two sets of RV measurements as separate instruments. Among all post-upgrade HIRES RVs, we exclude one relative RV ($-11.0 \pm 7.8 \, \mathrm{m \, s^{-1}}$) observed on 2005 July 17 UT (Sozzetti et al. 2009). This relative RV measurement lines up with the trend established by the pre-upgrade RVs but is 9σ lower than the extrapolated value ($64.3 \pm 1.5 \, \mathrm{m \, s^{-1}}$) from the RV measurements over 2012–2016, suggesting that the measurement made in 2005 has a different RV zero-point (ZP). We also exclude one relative RV ($-27.30 \pm 1.98 \, \mathrm{m \, s^{-1}}$) observed on 2013 July 21 UT (Butler et al. 2017), which is 14σ lower than the other relative RVs measured within 2 yr (Figure 2). The remaining 161 post-upgrade HIRES RVs exhibit a slope of $-8.0 \pm 0.2 \, \mathrm{m \, s^{-1} \, yr^{-1}}$ (rms = $3.1 \, \mathrm{m \, s^{-1}}$). The four pre-upgrade HIRES RV measurements show a linear trend of $-14.0 \pm 7.0 \, \mathrm{m \, s^{-1} \, yr^{-1}}$ (rms = $1.9 \, \mathrm{m \, s^{-1}}$). The combined HRS and HIRES data comprise 185 RVs together, spanning a baseline of 12 yr.

3.4. Relative RV between BC and A

We perform a reanalysis of the Keck I/HIRES spectra of Kepler-444 BC that were used by Dupuy et al. (2016) to measure absolute RVs of both B and C components. Multiepoch absolute RVs of the individual binary components can constrain the systemic RV of this binary. Comparing the absolute RV of the Kepler-444 BC system to that of Kepler-444 A, Dupuy et al. (2016) measured the orbital speed orthogonal to the plane of the sky and used this in their orbit analysis. Our reanalysis was originally motivated by a discrepancy in our own orbital analysis and that of
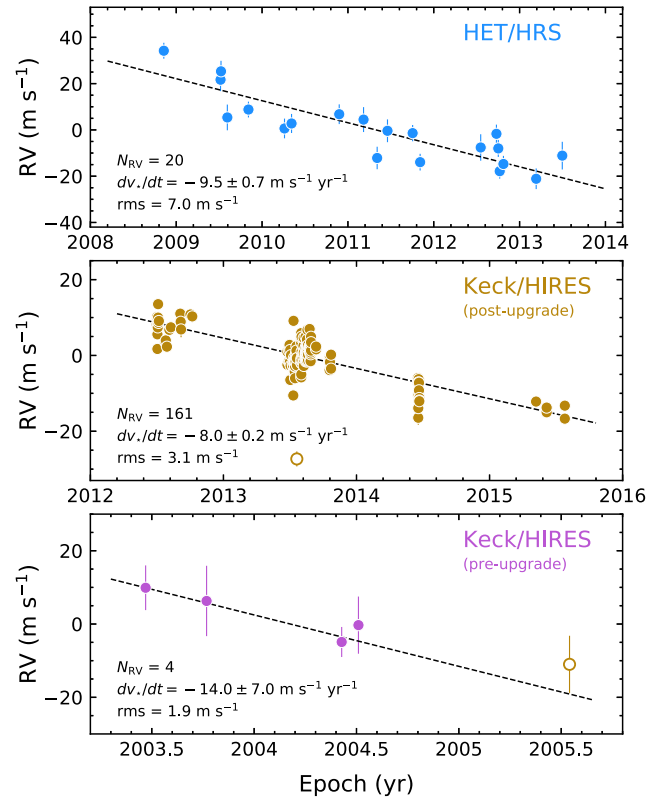
Figure 2. Multiepoch relative RVs of Kepler-444 A measured from HET/HRS (top) in this work and from Keck/HIRES after (middle) and before (bottom) the CCD upgrade on 2004 August 18 UT by Sozzetti et al. (2009), Dupuy et al. (2016), and Butler et al. (2017). We use open circles to mark two relative RV measurements excluded from our analysis (see Section 3.3). Linear fits of relative RVs are shown as dashed lines, and we label the fitted RV slopes and rms, as well as the total number of RV measurements used in our orbit analysis.

Dupuy et al. (2016) with the sign and possibly the amplitude of the BC−A relative RV, i.e., $\Delta RV_{BC-A} = RV_{BC} - RV_A$. We also include one additional HIRES spectrum of Kepler-444 BC, so our reanalysis uses a total of four epochs of BC's RV measurements.

All spectra were obtained in the standard setup of the California Planet Search (Howard et al. 2010), which provides consistent wavelength solutions for the three chips.[13] To define RV ZPs, we

---

[13] https://exoplanets.caltech.edu/cps/hires/

Table 3
Absolute Radial Velocities of Kepler-444 BC

Epoch (JD)	RV_B (km s^{-1})	RV_C (km s^{-1})
2,456,524.75034	-117.78 ± 0.11	-130.85 ± 0.09
2,456,532.74431	-115.46 ± 0.08	-133.88 ± 0.12
2,456,844.98015	-136.11 ± 0.10	-112.50 ± 0.09
2,457,229.93446	-131.56 ± 0.10	-116.54 ± 0.19

use the HIRES spectrum of the RV standard Barnard's star (-110.11 km s^{-1}; Fouqué et al. 2018), its barycentric correction of -22.75 km s^{-1}, and the barycentric corrections of Kepler-444 BC over the four epochs of -5.39, -7.04, 4.38, and -0.02 km s^{-1}, respectively. For each spectral order, we interpolate the science spectrum and the standard spectrum onto a common wavelength grid, which is uniform in $\log(\lambda)$ and has the same number of pixels as the input spectra. We then use the cross-correlation procedure C_CORRELATE in IDL to compute the wavelength differences in pixels between Kepler-444 BC and the standard. To convert this pixel shift into RV, we use the median pixel size of 1.29–1.31 km s^{-1} pixel^{-1}. We fit the cross-correlation functions as the sum of two Gaussians, each with its own position, amplitude, and standard deviation, plus a linearly sloped background. The best-fit model is derived using the Levenberg–Marquardt algorithm implemented in IDL by the MPFIT routine for IDL (Markwardt 2009). Given that not all HIRES orders provide well-defined double-peaked cross-correlation functions, we only use the best five orders from the red chip in our analysis (orders 1, 3, 4, 5, and 8). Finally, we determine RV_B as the position of the higher Gaussian peak and RV_C as that of the lower peak. Table 3 summarizes our resulting RVs, where we quote the means and, for error bars, the standard deviations across the different HIRES orders.

Comparing our newly derived absolute RVs to those reported in Dupuy et al. (2016), we find excellent agreement in the RV differences between B and C, but the ZPs are slightly different by $\approx$1–2 km s^{-1}. We believe that this is most likely due to small systematic errors (1%–2%) in the pixel scale used in the previous analysis because the ZP offset is the largest at the epochs where the difference in pixels between the standard star and science target is also the largest.

Following Wilson (1941), we convert BC's multiepoch RVs into the systemic velocity RV_{BC} and the C-to-B mass ratio q_{C-B} based on this expression:

$$RV_B = -q_{C-B} \times RV_C + RV_{BC} \times (1 + q_{C-B}). \quad (3)$$

We perform an orthogonal distance regression to incorporate the RV uncertainties of each component (Figure 3) and derive $RV_{BC} = -124.35 \pm 0.11$ km s^{-1}, leading to a BC$-$A relative RV of $\Delta RV_{BC-A} = RV_{BC} - RV_A = -3.1 \pm 0.2$ km s^{-1} during the HIRES observations that span 1.9 yr. Given that ΔRV_{BC-A} is periodically changing within a full barycentric orbit of Kepler-444 BC, we estimate its time derivative based on A's RV acceleration as

$$\frac{d}{dt}(\Delta RV_{BC-A}) = \frac{d}{dt}(RV_{BC} - RV_A)$$
$$= \frac{d}{dt}\left(-\frac{M_A}{M_{BC}}RV_A - RV_A\right)$$
$$= -\frac{M_A + M_{BC}}{M_{BC}} \times \frac{d}{dt}(RV_A). \quad (4)$$

The absolute values of Kepler-444 A's RV acceleration are below 20 m s^{-1} yr^{-1} (Section 3.3). By assuming a very conservative BC-to-A mass ratio[14] of 0.6, we estimate that ΔRV_{BC-A} increases by <0.1 km s^{-1} over the 1.9 yr HIRES observations, and this change is smaller than the measured ΔRV_{BC-A} uncertainty. Therefore, we adopt a mean epoch of 2,456,783.1 JD for this BC$-$A relative RV and include this single-epoch measurement in our subsequent orbit analysis. We have also determined the C-to-B mass ratio as $q_{C-B} = 0.967 \pm 0.024$ (Figure 3), leading to the first individual dynamical masses for B and C components (see Section 4).

4. Orbit Analysis

We use orvara (Brandt et al. 2021) to constrain the barycentric orbit and the dynamical mass of Kepler-444 BC by combining the system's relative astrometry, Hipparcos-Gaia absolute astrometry, Kepler-444 A's multiepoch RVs, and the single-epoch BC–A relative RV (Section 3). We use the parallel-tempering Markov Chain Monte Carlo (MCMC) sampler (Foreman-Mackey et al. 2013; Vousden et al. 2016) and run 50 temperatures and 100 walkers over 10^6 steps (per walker) to fit for 17 free parameters, including the masses of Kepler-444 A (M_A) and BC (M_{BC}), semimajor axis of the system (a), eccentricity (e), inclination (i), argument of the periastron of the primary star's orbit ($\omega_\star$), position angle of the ascending node (Ω), mean longitude of the primary star's orbit at epoch J2010.0 (i.e., 2,455,197.5 JD; $\lambda_{ref,\star}$), the marginalized parallax (ϖ) and barycentric proper motion ($\mu_\alpha \cos\delta$ and μ_δ) of the system, and three combinations of the RV jitter (σ_{jit}) and RV ZP for the HET/HRS, pre-upgrade Keck/HIRES, and post-upgrade Keck/HIRES data sets.[15] We save the chains every 50 steps and remove the first 5000 samples from each walker of the thinned chains as burn-in.

We set a Gaussian prior for the primary star's mass as $M_A = 0.75 \pm 0.03$ $M_\odot$, which is derived by Buldgen et al. (2019) using the same stellar oscillation frequencies but the updated stellar spectrophotometric properties and different sets of evolution models from those in Campante et al. (2015). This derived mass is also consistent with those in previous studies (e.g., Campante et al. 2015; Mack et al. 2018; Bellinger et al. 2019). In Appendix A, we demonstrate that our fitted orbital parameters remain nearly unchanged if we adopt a broader prior on the mass of Kepler-444 A as 0.75 ± 0.15 $M_\odot$. Log-flat priors are used for M_{BC}, a, and σ_{jit} (constrained between 10^{-5} and 10 m s^{-1}), and an isotropic distribution prior is assumed for i. Uniform priors are used for $\sqrt{e}\sin\omega_\star$, $\sqrt{e}\cos\omega_\star$, Ω, $\lambda_{\star,ref}$, $\mu_\alpha\cos\delta$, μ_δ, and RV ZPs. A Gaussian prior is set for ϖ with the mean and standard deviation from Gaia EDR3 (27.358 ± 0.013 mas).

Figure 4 presents the resulting parameter posteriors and the fitted sky-projected orbits of Kepler-444. We compare the observed relative astrometry, absolute astrometry, and RVs to model predictions in Figure 5. The fitted and derived physical properties and uncertainties are listed in Table 4. The entire set

---

[14] Our orbit analysis has determined the dynamical mass of Kepler-444 BC with a BC-to-A mass ratio of 0.81 ± 0.04 (Section 4 and Table 4). In addition, Dupuy et al. (2016) derived a ratio of 0.71 ± 0.07 by comparing Kepler-444 BC's photometry-based mass and the Kepler-444 A's asteroseismic mass.
[15] All orbital parameters correspond to the secondary's orbit unless noted. In addition, e and $\omega_\star$ are implicitly fitted as $\sqrt{e}\sin\omega_\star$ and $\sqrt{e}\cos\omega_\star$ following the convention of orvara.
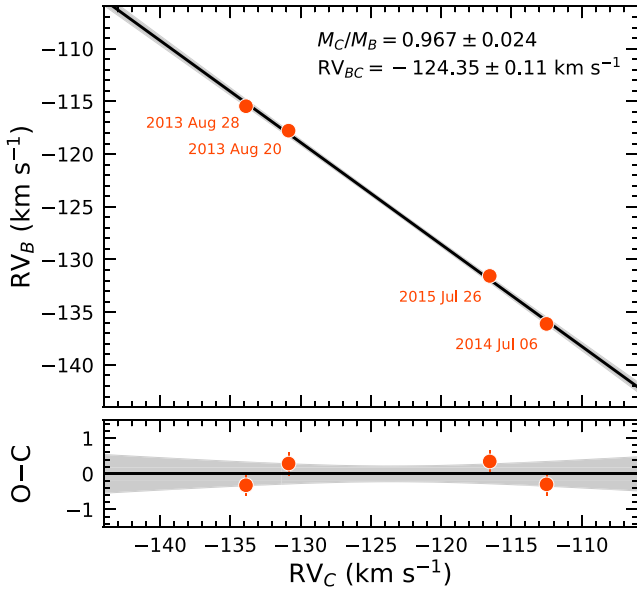
Figure 3. Top: absolute RVs of Kepler-444 B and C components (orange circles; Table 3), overlaid with the fitted model (black) and the 1σ interval (gray) as described in Equation (3). Bottom: the observed$-$calculated (i.e., $O-C$) residuals.

of MCMC chains of this orbit analysis presented here and those in the Appendix A and B are accessible online.[16]

Our analysis provides the latest characterization of the Kepler-444 system's architecture based on a uniform reanalysis of all published data and new observations. Compared to Dupuy et al. (2016), our newly derived semimajor axis of the system is 5σ larger, $a = 52.2^{+3.3}_{-2.7}$ au (compared to $36.7^{+0.7}_{-0.9}$ au), and the eccentricity is 5.7σ smaller, $e = 0.55 \pm 0.05$ (compared to 0.86 ± 0.02). These updates lead to a wider relative separation between A and BC during the periastron and imply a much larger size and mass of the truncated protoplanetary disk of Kepler-444 A (Section 5.1). The new inclination is consistent with the previous analysis, although our updated value is 8.5 times more precise, $i = 85°.4^{+0.3}_{-0.4}$ (compared to $90°.4^{+3.9}_{-3.6}$). Therefore, we draw the same conclusion as Dupuy et al. (2016) that there is a possible orbital alignment between the stellar binary and transiting planets (Section 5.2). In addition, $\omega_\star$ is $\approx 120°$ lower and Ω is $\approx 180°$ higher, suggesting a different three-dimensional orientation of BC's barycentric orbit.

We further measure the individual dynamical masses of Kepler-444 B and C for the first time, given that their total mass is well constrained by our orbit analysis and the C-to-B mass ratio has been measured from multiepoch absolute RVs of these two components (Section 3.4). We find $M_B = 0.307^{+0.009}_{-0.008}\ M_\odot$ and $M_C = 0.296 \pm 0.008\ M_\odot$, with 2σ intervals and best-fit values, as listed in Table 4.

In addition, the relative RV between the primary and secondary components is not a common observable in the orbit analysis of stellar binaries, especially when the binary has a tight angular separation. To test the importance of this observable, we re-perform the orbit analysis by excluding the BC$-$A relative RV (Appendix B). Without ΔRV$_{BC-A}$, we find that the resulting parameter posteriors would be composed of two families of orbital solutions with similar shapes (e.g.,

---

semimajor axis and eccentricity) and line-of-sight inclinations but completely different three-dimensional orientations. This analysis thus reveals the power of an even single-epoch relative RV between the primary and the secondary in order to precisely and accurately constrain the architecture of stellar binaries (e.g., Pearce et al. 2020), especially when the secondary is near the apoapsis on a long-period orbit like Kepler-444.

5. Discussion

5.1. The Truncated Protoplanetary Disk of Kepler-444 A

The protoplanetary disk of Kepler-444 A was likely truncated by BC during the early evolutionary stages of this system (see Zeng et al. 2022 for a similar example). Therefore, the periastron separation between A and BC provides a boundary condition on the size and mass of this truncated disk. Based on an inferred periastron separation of $5.0^{+0.9}_{-1.0}$ au, Dupuy et al. (2016) estimated that A's disk likely had a radius of 2 au, with a dust mass of $4\ M_\oplus$ if the disk gas surface density follows the minimum-mass solar nebula (MMSN). Their results imply that the primary star's disk would be too heavily depleted of solids to support the formation of five rocky planets unless the dust-to-planet conversion is very efficient or the disk surface density is slightly higher than the MMSN.

Here we reexamine the properties of Kepler-444 A's truncated disk using our new orbital parameters, which imply a 4.6 ± 1.2 times wider periastron separation between A and BC of 23 ± 4 au (Table 4). Artymowicz & Lubow (1994) performed an analytical study of disk$-$binary interactions and estimated the size of truncated circumprimary, circumsecondary, and circumbinary disks using the disk radius at which the resonant torque (from interactions between the disk and eccentric binary orbits) and the viscous torque (within the disk) are balanced. They computed truncated disk radii as functions of the mass ratio between binary components, the secondary's orbital eccentricity, and the disk viscosity (described by the Reynolds number $\mathcal{R}$), assuming that the stellar binary and the disk are perfectly aligned. Manara et al. (2019) further expanded the numerical simulation results of Artymowicz & Lubow (1994) into analytical functions, with the truncated radius of the circumprimary disk expressed as

$$R_{disk,pri} = a \times \frac{0.49 \times q^{2/3}}{0.6 \times q^{2/3} + \ln(1 + q^{1/3})}$$
$$\times (b \times e^c + 0.88\mu^{0.01}), \tag{5}$$

where a is the system's semimajor axis, e is the eccentricity of the secondary's orbit, $q = M_{pri}/M_{sec}$ is the primary-to-secondary mass ratio, and $\mu = M_{sec}/(M_{pri} + M_{sec})$ is the secondary-to-total mass ratio. Here b and c are parameters that depend on μ and $\mathcal{R}$ (see Table C.1 in Manara et al. 2019). The truncated radius of the circumsecondary disk is expressed by the same equation, with q switched to the secondary-to-primary mass ratio M_{sec}/M_{pri}.

Given that Kepler-444 has $\mu = 0.45 \pm 0.01$ based on our orbit analysis, we compute Kepler-444 A's disk radius using several combinations of b and c corresponding to $\mu = 0.4$ or 0.5, and $\mathcal{R} = 10^4$, 10^5, or 10^6. The resulting disk radii span 7–9 au with a typical uncertainty of ≈ 1 au. In addition, the barycentric orbit of Kepler-444 BC and those of Kepler-444 A's transiting planets have mutual inclinations of at least

---

[16] https://github.com/zjzhang42/Kepler_444_orbit_analysis
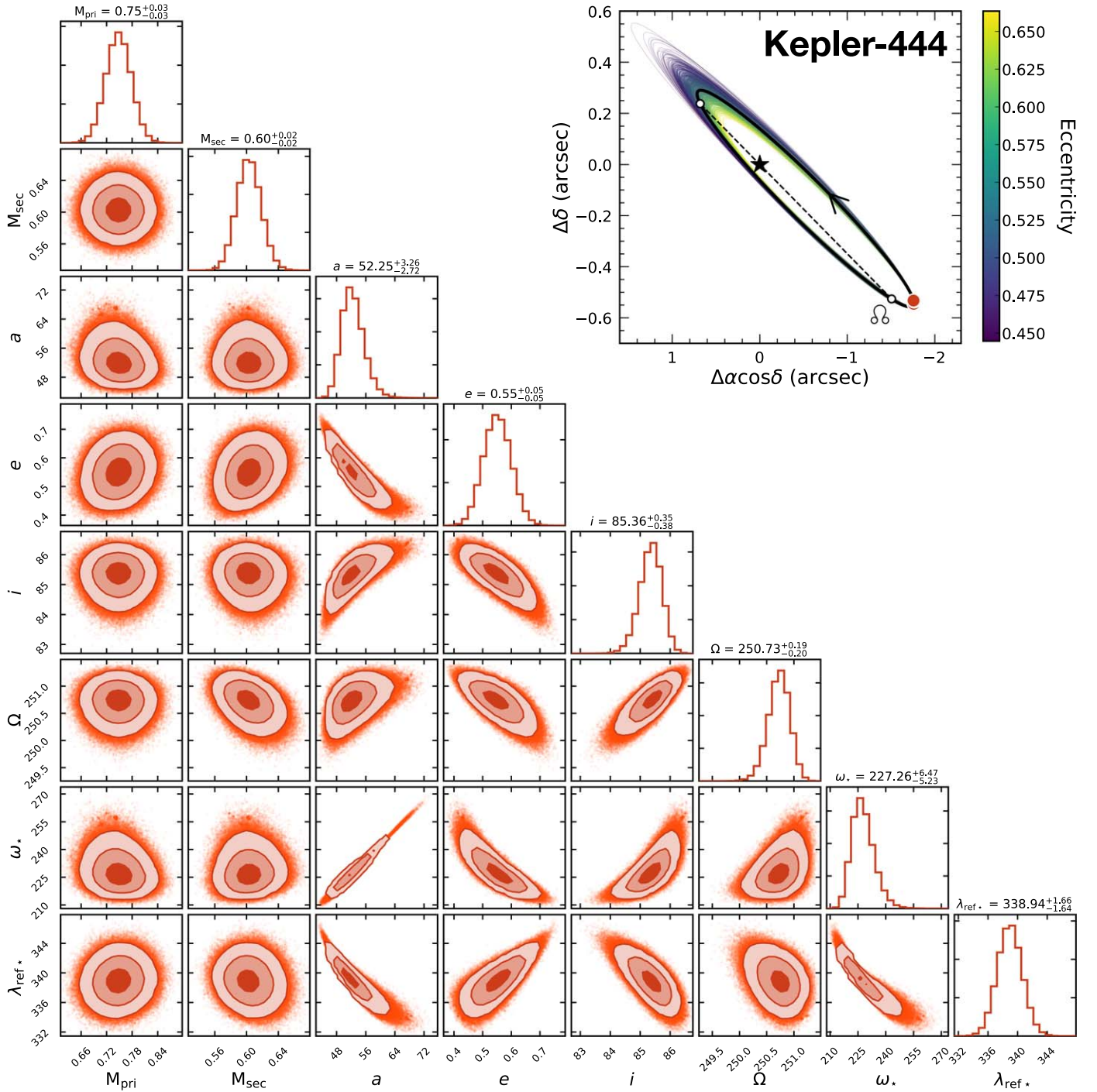
Figure 4. Posteriors from our orbit analysis of Kepler-444. Details about each parameter, including credible intervals and the best-fit values of these parameters, are listed in Table 4. The top right panel shows the predicted relative astrometry between the A and BC components based on 1000 randomly drawn orbits from the MCMC chains, here color-coded by eccentricity. The black solid line shows the best-fit orbit. The two white circles mark the ascending node (i.e., the point in BC's orbit in which it is moving toward the observer through the sky plane; labeled) and the descending node connected via a dashed line (i.e., the line of nodes). Kepler-444 A is shown as a black star, and the observed relative astrometry of BC traces out the orbital arc at the bottom right.

$1°6$–$4°6$ (Section 5.2), and if this misalignment is primordial, then Kepler-444 slightly deviates from the coplanarity assumption of Artymowicz & Lubow (1994) embedded in Equation (5). As suggested by Lubow et al. (2015), circumprimary or circumsecondary disks that are misaligned with the stellar binary orbit by ψ can have systematically larger radii compared to those of aligned disks, as the resonant torque on the disk decays as $\cos^8(\psi/2)$ (also see Miranda & Lai 2015).

Therefore, we adopt a conservative truncation radius of 8 au, which is 4 times larger than Dupuy et al. (2016).

We follow the same method as Dupuy et al. (2016) to estimate the potential reservoir of dust mass that resided in Kepler-444 A's disk. Specifically, we integrate an MMSN gas surface density of $\Sigma(r) = 1700 \times (r/1 \text{ au})^{3/2}$ g cm^{-2} (Weidenschilling 1977; Hayashi 1981) using our estimated truncation disk radius and a dust-to-gas mass ratio of 1:300 (to
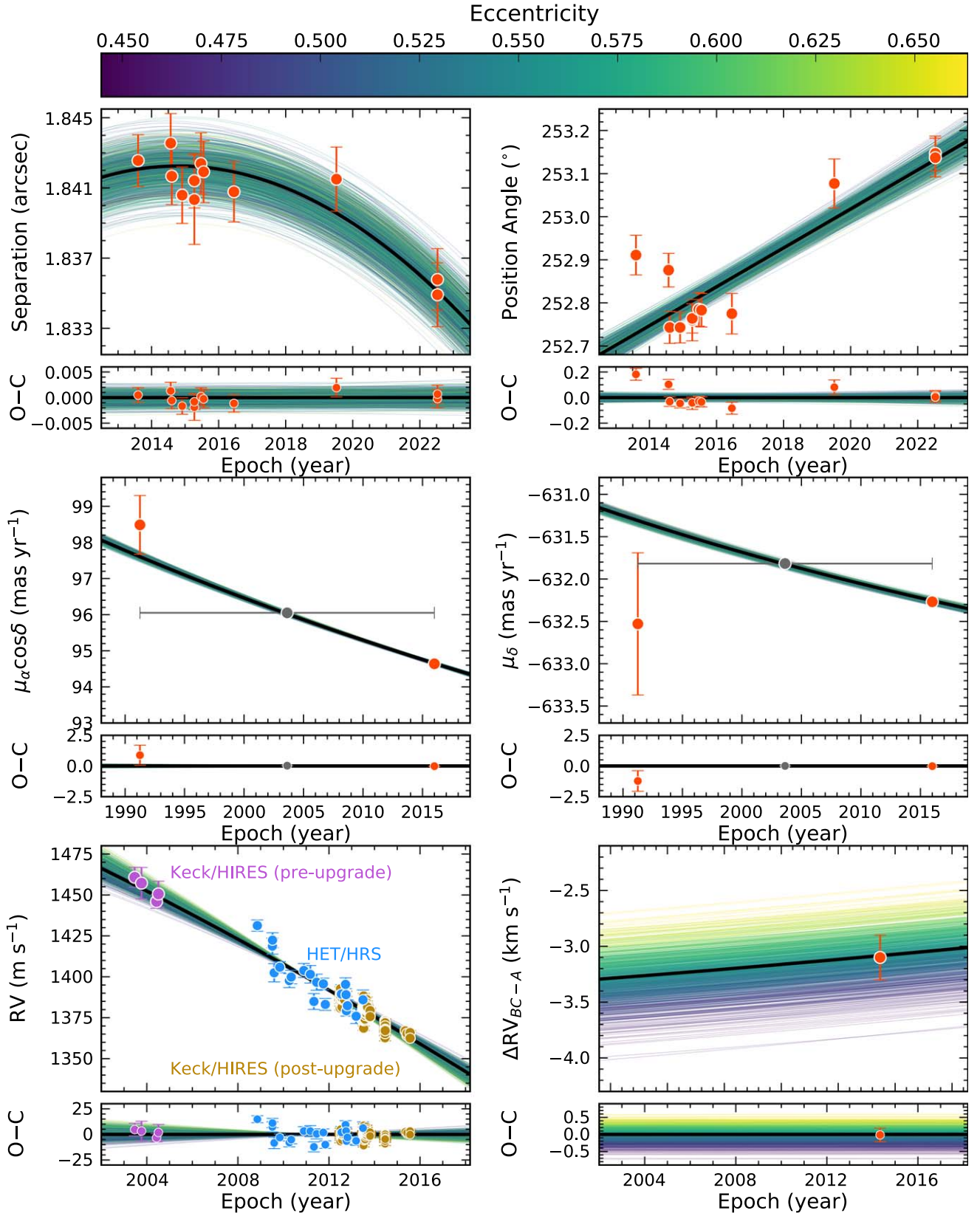
Figure 5. Model predictions overlaid on the observed relative astrometry from Keck/NIRC2 (top), absolute astrometry from Hipparcos (J1991.25) and Gaia EDR3 (J2016; middle), Kepler-444 A's multiepoch RVs from HET/HRS and Keck/HIRES (bottom left), and the single-epoch BC–A relative RV from Keck/HIRES (bottom right). In each panel, we show the observed data (upper) and residuals (lower) using orange circles, except (1) the middle panels, where we use gray circles to present the weighted-mean proper motion between Hipparcos and Gaia at J2003.625, the value that `orvara` uses to constrain the model-predicted proper motions of Kepler-444 A (Brandt et al. 2021); and (2) the bottom left panel, where we use different colors to label RVs collected by different instruments. Predictions of 1000 randomly drawn orbits from the MCMC trials are overlaid in each panel color-coded by eccentricities. Predictions from the best-fit orbit are shown as black solid lines.

Table 4
Orbit Analysis of Kepler-444

Parameter[a]	Unit	Median $\pm 1\sigma$	2σ Confidence Interval	Best Fit	Adopted Prior
		Fitted Parameters			
Mass of Kepler-444 A, M_A	$M_\odot$	$0.75^{+0.03}_{-0.03}$	(0.69, 0.81)	0.74	$\mathcal{N}(\mu = 0.75, \sigma^2 = 0.03^2)$
Mass of Kepler-444 BC, M_{BC}	$M_\odot$	$0.60^{+0.02}_{-0.02}$	(0.57, 0.63)	0.60	$1/M$ (log-flat)
Semimajor axis, a	au	$52.2^{+3.3}_{-2.7}$	(47.2, 59.4)	52.0	$1/a$ (log-flat)
$\sqrt{e}\sin\omega_\star$	...	$-0.55^{+0.03}_{-0.03}$	(−0.61, −0.48)	−0.54	Uniform
$\sqrt{e}\cos\omega_\star$	...	$-0.50^{+0.08}_{-0.07}$	(−0.63, −0.32)	−0.51	Uniform
Inclination, i	deg	$85.4^{+0.3}_{-0.4}$	(84.5, 86.0)	85.3	$\sin(i)$ with $i \in [0, 180°]$
PA of the ascending node, Ω	deg	$250.7^{+0.2}_{-0.2}$	(250.3, 251.1)	250.7	Uniform
Mean longitude at J2010.0, $\lambda_{ref,\star}$	deg	$338.9^{+1.7}_{-1.6}$	(335.7, 342.3)	339.2	Uniform
Parallax, ϖ	mas	$27.358^{+0.016}_{-0.016}$	(27.325, 27.391)	27.361	$\mathcal{N}(\mu = 27.358, \sigma^2 = 0.013^2)$
System barycentric proper motion in R.A., $\mu_\alpha\cos(\delta)$	mas yr^{-1}	$94.58^{+0.03}_{-0.03}$	(94.52, 94.63)	94.59	Uniform
System barycentric proper motion in decl., μ_δ	mas yr^{-1}	$-631.61^{+0.04}_{-0.04}$	(−631.68, −631.53)	−631.60	Uniform
RV jitter for HET/HRS, $\sigma_{jit,HRS}$	m s^{-1}	$6.2^{+1.6}_{-1.3}$	(3.6, 9.3)	5.4	$1/\sigma_{jit,HRS}$ (log-flat)
RV ZP for HET/HRS, ZP_{HRS}	m s^{-1}	1408^{+96}_{-94}	(1221, 1601)	1397	Uniform
RV jitter for post-upgrade HIRES, $\sigma_{jit,post-HIRES}$	m s^{-1}	$2.9^{+0.2}_{-0.2}$	(2.5, 3.3)	2.9	$1/\sigma_{jit,post-HIRES}$ (log-flat)
RV ZP for post-upgrade HIRES, $ZP_{post-HIRES}$	m s^{-1}	1390^{+95}_{-94}	(1203, 1583)	1379	Uniform
RV jitter for pre-upgrade HIRES, $\sigma_{jit,pre-HIRES}$	m s^{-1}	$0.0^{+0.7}_{-0.0}$	(0.0, 5.3)	0.0	$1/\sigma_{jit,pre-HIRES}$ (log-flat)
RV ZP for pre-upgrade HIRES, $ZP_{pre-HIRES}$	m s^{-1}	1463^{+96}_{-94}	(1275, 1657)	1451	Uniform
		Derived Parameters			
Mass of Kepler-444, B M_B	$M_\odot$	$0.307^{+0.009}_{-0.008}$	(0.290, 0.324)	0.308	...
Logarithmic mass of Kepler-444 B, $\log(M_B/M_\odot)$	...	$-0.514^{+0.012}_{-0.012}$	(−0.538, −0.489)	−0.511	...
Mass of Kepler-444 C, M_C	$M_\odot$	$0.296^{+0.008}_{-0.008}$	(0.280, 0.314)	0.297	...
Logarithmic mass of Kepler-444 C, $\log(M_C/M_\odot)$	...	$-0.528^{+0.012}_{-0.012}$	(−0.553, −0.504)	−0.527	...
BC-to-A mass ratio, M_{BC}/M_A	...	$0.81^{+0.04}_{-0.04}$	(0.73, 0.89)	0.80	...
Eccentricity, e	...	$0.55^{+0.05}_{-0.05}$	(0.46, 0.65)	0.55	...
Argument of periastron, $\omega_\star$	deg	$227.3^{+6.5}_{-5.2}$	(217.7, 241.7)	226.6	...
Period, P	yr	324^{+31}_{-25}	(277, 396)	323	...
Time of periastron, T_0[b]	JD	2537060^{+10881}_{-8533}	(2521634, 2562059)	2536428	...
On-sky semimajor axis, $a \times \varpi$	mas	1429^{+89}_{-74}	(1291, 1625)	1422	...
Minimum A−BC separation, $a(1-e)$	au	23^{+4}_{-4}	(17, 32)	23	...

Notes.
[a] Orbital parameters all correspond to Kepler-444 BC except for a, $\omega_\star$, and $\lambda_{ref,\star}$. The first parameter corresponds to the system's (instead of individual components') semimajor axis, and the latter two parameters correspond to those of Kepler-444 A's orbit.
[b] T_0 is computed as $t_{ref} - P \times (\lambda_{ref,\star} - \omega_\star)/360°$, where $t_{ref} = 2{,}455{,}197.5$ JD (i.e., epoch J2010.0).

incorporate the primary star's low metallicity of [Fe/H] $= -0.52 \pm 0.12$ dex; Mack et al. 2018). This leads to $500\,M_\oplus$ or $1.6\,M_{Jup}$, implying a much larger potential mass reservoir of dust as compared to the value of $4\,M_\oplus$ derived in Dupuy et al. (2016) under the same assumption of an MMSN disk. With a truncated disk radius of 2 au, Dupuy et al. (2016) suggested that a $\approx 20\times$ denser MMSN would be sufficient to explain the planet formation and such a disk would have a mass of 80–240 $M_\oplus$ depending on the dust-to-gas mass ratio. We find that these values are closer to our new estimate of the disk dust mass.

In addition to a more massive truncated disk of Kepler-444 A, we also update the estimates of planet masses. Dupuy et al. (2016) derived a total mass of $1.5\,M_\oplus$ for A's five planets based on these objects' measured radii and the Lissauer et al. (2011) mass–radius relation of $(M/M_\oplus) \sim (R/R_\oplus)^{2.06}$. After this study, Mills & Fabrycky (2017) used transit timing variation to directly constrain the photodynamical masses of Kepler-444 d and e to be $0.036^{+0.065}_{-0.020}\,M_\oplus$ and $0.034^{+0.059}_{-0.019}\,M_\oplus$, respectively. These measurements suggest that planets d and e likely have water-rich or pure-rock compositions. These

directly measured masses are 7 times smaller than those estimated by Dupuy et al. (2016). This discrepancy is likely because the Lissauer et al. (2011) mass–radius relation was determined with Earth and Saturn, which have much larger densities than Kepler-444 A's planets. Using a mass–radius relation of $(R/R_\oplus) \sim (M/M_\oplus)^{0.28}$ by Chen & Kipping (2017) for "Terran worlds" (with radii of 0.1–1 $R_\oplus$), we find that the predicted masses of d (0.104 $M_\oplus$) and e (0.115 $M_\oplus$) at their radii are about 3 times higher than the measured masses. Regardless, assuming that Kepler-444 bcf planets all follow the Chen & Kipping (2017) Terran-world mass–radius relation, we compute their masses to be 0.039, 0.082, and 0.343 $M_\oplus$, respectively, leading to a total mass of $0.53\,M_\oplus$ for Kepler-444 planets. This total mass drops to $0.22\,M_\oplus$ if the masses of b, c, and f are also 3 times smaller than the scaling-relation predictions as seen in d and e.

With our updated estimates about the disk's and planets' masses, Kepler-444's total planet mass within a given disk radius is well below the encompassed total disk dust mass. These planets' masses are still slightly higher than the predicted isolation mass of solids (i.e., the maximum available mass

reservoir needed for planets to undergo runaway accretion; Lissauer 1987) at their currently observed locations in an MMSN disk (e.g., see Figure 6 of Dupuy et al. 2016). Thus, it is likely that the disk surface density of Kepler-444 A is only slightly ($\approx 4\times$) higher than the MMSN. In addition, given that the truncated disk of Kepler-444 A is three orders of magnitude more massive than the currently observed planet masses, it is possible that Kepler-444 A's planets—tightly packed within 0.1 au—built their masses by accreting pebbles delivered from larger disk radii (e.g., Chatterjee & Tan 2014; Lee et al. 2014), as discussed in Dupuy et al. (2016). Therefore, we conclude that the previously noticed tension between Kepler-444 A's disk mass and its planet masses is now resolved by the new orbit analysis of this system.

5.2. Mutual Inclinations between the Barycentric Orbit of Kepler-444 BC and Orbits of the Kepler-444 A Planets

Mutual inclinations between Kepler-444 BC's barycentric orbit and the orbits of Kepler-444 A's planets provide valuable insight into the impact of stellar binaries on the formation and evolution of planets (e.g., Czekala et al. 2019; Christian et al. 2022; Dupuy et al. 2022). Deriving this mutual inclination ψ requires knowledge of the inclination i and the position angle of the ascending node for orbits of both the outer binary (B) and the inner planet (p):

$$\psi = \cos^{-1}[\cos(i_p)\cos(i_B) + \sin(i_p)\sin(i_B)\cos(\Omega_p - \Omega_B)].$$
(6)

Given that Ω_p is usually unknown for transiting planets, only the minimum value of ψ can be constrained as $|i_p - i_B|$ (e.g., Bowler et al. 2017). Our derived inclination of Kepler-444 BC is $85.4^{+0.3}_{-0.4}$, and the observed inclinations of A's five planets span $87°–90°$ (Campante et al. 2015). Therefore, the true mutual inclination can be as small as $\psi = 1.6–4.6$. This result is consistent with Dupuy et al. (2016), who derived $i_B = 90.4^{+3.4}_{-3.6}$, leading to a minimum $\psi = 0.4–3.4$.[17]

The mutual inclination could be significantly large if the orbital ascending node of BC's barycenter and those of planets have different position angles. However, if the orbital plane of BC–A and that of A's planets have large mutual inclinations, then the torque of the misaligned barycentric orbit of BC on the planets could cause the planets to precess as a rigid disk, which in turn would lead to cases where between none to all five planets are transiting along the line of sight (e.g., Dupuy et al. 2016). Therefore, it is likely that the orbital plane of BC–A and that of the planets are nearly aligned. As extensively discussed in Dupuy et al. (2016), the potential coplanarity of the stellar and the planet orbits in the Kepler-444 system might be explained if they all formed within a large circumstellar disk, which fragmented to form the BC binary pair during the early evolutionary stages of the system and then subsequently

formed the planets through core accretion at some later stage (e.g., Adams et al. 1989; Bonnell & Bate 1994; Kratter & Lodato 2016; Tobin et al. 2016; Tokovinin 2018; Offner et al. 2022). Alternatively, the planet−binary coplanarity might also be a result of turbulent fragmentation, with BC having a primordial misalignment with A's protoplanetary disk. The disk could be torqued to precess by BC, with the energy dissipation driving the disk toward the aligned configuration (e.g., Bate et al. 2000; Batygin 2012; Zanazzi & Lai 2018; Christian et al. 2022).

It is noteworthy to compare our derived planet−binary mutual inclination of Kepler-444 with other observational evidence about the statistical alignment between stellar binaries and their planets. Christian et al. (2022) studied 67 host stars of candidate transiting planets identified by the Transiting Exoplanet Survey Satellite (TESS; Ricker et al. 2015), which have outer stellar companions. They found that the measured orbital inclinations of the planet host stellar binaries (particularly those with semimajor axes below 700 au) are preferentially closer to i_p (assumed to be $90°$), while the inclinations of binaries without planets follow an isotropic distribution. The overabundance of small $|i_p - i_b|$ (or $|90° - i_b|$) in their samples thus points to a possible binary−planet alignment, given that these systems' Ω_p should be independent from i_p or i_b.

In addition, Dupuy et al. (2022) studied 45 planet host stellar binaries and defined a metric γ, which is the angle between the secondary's on-sky orbital speed along the position angle (i.e., tangential) direction and that along the separation direction. Based on their definition, γ is close to $0°$ when the orbital motion along the tangential direction is zero, implying an edge-on orbit of the secondary and thereby a small ψ between the binaries' and planets' orbits. The observed γ distribution in their work is skewed toward $0°$ and is best explained if orbits of stellar binaries and their planets are aligned within $30°$ and if these binaries have uniformly distributed eccentricities within 0.1−0.8 (similar to those of field binaries; Raghavan et al. 2010).

In addition, Behmard et al. (2022) studied 168 host stars of TESS candidate transiting planets with outer stellar companions. Similar to Dupuy et al. (2022), they independently defined a metric γ that measures the angle between a stellar binary's relative position vector and relative proper-motion vector, as a probe of the planet−binary mutual inclination. Among a subset that host sub-Neptune or super-Earth planets (with planets' $a < 1$ au and radii $\leqslant 4\,R_\oplus$), they found that $73^{+14}_{-20}\%$ of this set has planet−binary mutual inclinations of $35° \pm 24°$. However, among a subset that hosts close-in gas-giant planets (with planets' orbital periods <10 days and radii $>4\,R_\oplus$), which are not characteristic of the planets in Kepler-444, they found that $65^{+20}_{-35}\%$ of these systems favor a perpendicular planet−binary mutual inclination of $89° \pm 21°$.

Therefore, the potential alignment between BC's barycentric orbit and the orbits of A's planets in the Kepler-444 system generally lines up with those of statistical samples. Direct constraints about the planet−binary mutual inclination have been rare in S-type planetary systems, largely due to the unknown Ω_p of inner planets. In contrast, such measurements have been carried out for protoplanetary disks surrounding short-period ($P \leqslant 35$ days) spectroscopic binaries (leading to small disk−binary mutual inclinations of $\leqslant 6°$; e.g., Czekala et al. 2019, 2021), as well as hierarchical stellar multiple systems (e.g., Borkovits et al. 2016; Tobin et al. 2016; Tokovinin 2018).

---

[17] In addition to the planet−binary mutual inclination, the inclination of Kepler-444 A's spin axis (i_A) was measured by Campante et al. (2016) using asteroseismology. Their inferred probability distribution of i_A peaks at $90°$, with wide 1σ and 2σ confidence intervals of $31.3°–90°$ and $22.7°–90°$, respectively. Given the large i_A uncertainty and unknown sky-projected obliquities of the planets and BC, it remains unclear whether A's stellar spin axis, the planets' orbits, and BC's barycentric orbit are (mis)aligned. In addition, an alignment was suggested by Hale (1994) among a close ($\lesssim 30$ au) stellar binary's orbit and stellar spin axes of binary components, although recent studies found that the existing data and precision are insufficient to assess the spin–orbit alignment of binaries (e.g., Justesen & Albrecht 2020).

6. Conclusion

We present the latest characterization of the architecture for the ancient ($\sim$11 Gyr) Kepler-444 system, which is composed of a metal-poor ($[\mathrm{Fe/H}] = -0.52 \pm 0.12$ dex) K0 primary star, Kepler-444 A, hosting five sub-Earth-sized transiting planets, and a tight M-type spectroscopic binary, Kepler-444 BC. Combining our new observations and previously published data, we measure the system's relative astrometry, the primary star's multiepoch RVs, and the BC$-$A relative RVs. We have also implemented the absolute astrometry and significant astrometric acceleration from Hipparcos and Gaia.

Our work has provided significant updates to the orbital parameters of Kepler-444 BC's barycentric orbit compared to the previous work (Dupuy et al. 2016), mainly because of our reanalysis of the BC$-$A relative RV and because our new observations have greatly extended the time baseline of the existing monitoring of the system's astrometry from 3 to 9 yr. These updates include a 5σ larger semimajor axis ($a = 52.2^{+3.3}_{-2.7}$ au), a 5.7σ smaller eccentricity ($e = 0.55 \pm 0.05$), a more precise orbital inclination ($i = 85°.4^{+0°.3}_{-0°.4}$), a $\approx 120°$ different argument of the primary star's periastron ($\omega_\star = 227°.3^{+6°.5}_{-5°.2}$), and a $\approx 180°$ different position angle of the A–BC ascending node ($\Omega = 250°.7 \pm 0°.2$). We have also measured the first individual dynamical masses for the B ($0.307^{+0.009}_{-0.008}\ M_\odot$) and C ($0.296 \pm 0.008\ M_\odot$) components.

The updated a and e of Kepler-444 BC's barycentric orbit lead to a 4.6 ± 1.2 times wider relative separation between A and BC during periastron passage, suggesting that the protoplanetary disk of Kepler-444 A was likely truncated to a radius of ≈ 8 au by tidal interactions of BC, with a total dust mass of $500\ M_\oplus$ assuming an MMSN disk. We also update the total mass of Kepler-444 A's planets to be $0.53\ M_\oplus$ by using the Chen & Kipping (2017) mass–radius relation and photodynamical mass measurements of Kepler-444 d and e (Mills & Fabrycky 2017). With our updated mass estimates of the truncated disk and planets, Kepler-444 A's five planets might have effectively built their masses via the accretion of pebbles delivered from larger disk radii if they formed in situ within a solid-depleted MMSN disk. This formation scenario was previously suggested by Dupuy et al. (2016), under an assumption of very efficient dust-to-planet conversion or a much higher disk surface density than MMSN, given the tension between their lower mass estimates of the disk ($4\ M_\oplus$) and higher mass estimates of the planets ($1.5\ M_\oplus$). This tension is now resolved by the new orbit analysis.

The updated inclination of Kepler-444 BC's barycentric orbit leads to the same conclusion as Dupuy et al. (2016) that the orbital plane of A–BC and those of the planets are consistent with being aligned, with the planet$-$binary mutual inclination as small as $1°.6$–$4°.6$. A misalignment is possible if the ascending nodes of these planets' orbits do not line up with that of BC but can cause situations where none to all five planets are transiting along the line of sight over the evolutionary history of this system. The coplanarity between the planets and the A–BC orbit might be explained if they all formed within a large circumstellar disk as extensively discussed in Dupuy et al. (2016) and lines up with recent statistical studies of planet host stellar binaries.

If we do not include the BC$-$A relative RV in our orbit analysis, then the resulting posteriors of orbital parameters are composed of two families of solutions, with comparable posterior probabilities and similar shapes but completely different three-dimensional orientations. Therefore, for systems like Kepler-444, it is important to observe even single-epoch relative RVs between the primary and the secondary in order to precisely and accurately constrain the binary orbital architecture, especially when the secondary is near apoapsis on a long-period orbit.

Appendix A
Orbit Analysis of Kepler-444 with a Broader M_A Prior

Here we investigate the impact of our adopted prior of Kepler-444 A's mass on the derived dynamical mass and barycentric orbit of Kepler-444 BC. In Section 4, we set a Gaussian prior of $0.75 \pm 0.03\ M_\odot$ for M_A based on the recent estimate by Buldgen et al. (2019), consistent with Campante et al. (2015), Mack et al. (2018), and Bellinger et al. (2019), who derived $M_A = 0.76 \pm 0.04\ M_\odot$, $0.76 \pm 0.01\ M_\odot$, and $0.75 \pm 0.01\ M_\odot$, respectively. The consistency of these measurements lines up with the expected small systematic error in

Table 5
Orbit Analysis of Kepler-444 with a Broader M_A Prior of $0.75 \pm 0.15\ M_\odot$

Parameter[a]	Unit	Median $\pm 1\sigma$	2σ Confidence Interval	Best Fit
		Fitted Parameters		
Mass of Kepler-444 A, M_A	$M_\odot$	$0.70^{+0.14}_{-0.14}$	(0.42, 0.98)	0.76
Mass of Kepler-444 BC, M_{BC}	$M_\odot$	$0.60^{+0.02}_{-0.02}$	(0.57, 0.63)	0.60
Semimajor axis, a	au	$53.1^{+4.7}_{-3.5}$	(47.0, 64.4)	52.3
$\sqrt{e}\sin\omega_\star$	...	$-0.55^{+0.04}_{-0.04}$	(−0.62, −0.48)	−0.54
$\sqrt{e}\cos\omega_\star$	...	$-0.48^{+0.12}_{-0.09}$	(−0.64, −0.20)	−0.50
Inclination, i	deg	$85.4^{+0.3}_{-0.4}$	(84.5, 86.0)	85.5
PA of the ascending node, Ω	deg	$250.7^{+0.2}_{-0.2}$	(250.3, 251.1)	250.8
Mean longitude at J2010.0, $\lambda_{ref,\star}$	deg	$338.7^{+1.8}_{-1.8}$	(335.2, 342.3)	338.8
Parallax, ϖ	mas	$27.358^{+0.016}_{-0.016}$	(27.325, 27.391)	27.363
System barycentric proper motion in R.A., $\mu_\alpha\cos(\delta)$	mas yr^{-1}	$94.58^{+0.03}_{-0.03}$	(94.52, 94.63)	94.57
System barycentric proper motion in decl., μ_δ	mas yr^{-1}	$-631.58^{+0.09}_{-0.08}$	(−631.72, −631.38)	−631.62
RV jitter for HET/HRS, $\sigma_{jit,HRS}$	m s^{-1}	$6.17^{+1.57}_{-1.34}$	(3.63, 9.30)	6.24
RV ZP for HET/HRS, ZP_{HRS}	m s^{-1}	1458^{+198}_{-166}	(1151, 1897)	1408
RV jitter for post-upgrade HIRES, $\sigma_{jit,post-HIRES}$	m s^{-1}	$2.88^{+0.20}_{-0.19}$	(2.52, 3.31)	2.83
RV ZP for post-upgrade HIRES, $ZP_{post-HIRES}$	m s^{-1}	1440^{+198}_{-165}	(1133, 1879)	1390
RV jitter for pre-upgrade HIRES, $\sigma_{jit,pre-HIRES}$	m s^{-1}	$0.01^{+0.72}_{-0.01}$	(0.00, 5.33)	2.08
RV ZP for pre-upgrade HIRES, $ZP_{pre-HIRES}$	m s^{-1}	1513^{+198}_{-166}	(1205, 1952)	1462
		Derived Parameters		
Mass of Kepler-444 B, M_B	$M_\odot$	$0.307^{+0.009}_{-0.008}$	(0.290, 0.324)	0.303
Logarithmic mass of Kepler-444 B, $\log(M_B/M_\odot)$	...	$-0.513^{+0.012}_{-0.012}$	(−0.538, −0.489)	−0.519
Mass of Kepler-444 C, M_C	$M_\odot$	$0.296^{+0.008}_{-0.008}$	(0.280, 0.314)	0.290
Logarithmic mass of Kepler-444 C, $\log(M_C/M_\odot)$	...	$-0.528^{+0.012}_{-0.012}$	(−0.553, −0.504)	−0.538
BC-to-A mass ratio, M_{BC}/M_A	...	$0.86^{+0.22}_{-0.15}$	(0.61, 1.45)	0.79
Eccentricity, e	...	$0.54^{+0.06}_{-0.06}$	(0.42, 0.66)	0.55
Argument of periastron, $\omega_\star$	deg	$228.8^{+9.4}_{-6.5}$	(217.4, 252.2)	227.2
Period, P	yr	338^{+62}_{-43}	(262, 496)	323
Time of periastron, T_0[b]	JD	$2541098^{+20089}_{-13351}$	(2518285, 2594167)	2536702
On-sky semimajor axis, $a \times \varpi$	mas	1451^{+127}_{-94}	(1284, 1762)	1429
Minimum A−BC separation, $a(1-e)$	au	$24.6^{+5.7}_{-4.6}$	(16.2, 37.3)	23.7

Notes.

[a] Orbital parameters all correspond to Kepler-444 BC except for a, $\omega_\star$, and $\lambda_{ref,\star}$. The first parameter corresponds to the system's (instead of individual components') semimajor axis, and the latter two parameters correspond to those of Kepler-444 A's orbit.

[b] T_0 is computed as $t_{ref} - P \times (\lambda_{ref,\star} - \omega_\star)/360°$, where $t_{ref} = 2{,}455{,}197.5$ JD (i.e., epoch J2010.0).

mass ($\lesssim 5\%$) inferred from different evolution and pulsation codes (e.g., Silva Aguirre et al. 2015; Cunha et al. 2021; Tayar et al. 2022). Nevertheless, to verify the robustness of our orbit analysis, here we assume a very conservative relative uncertainty of 20% for the primary star's mass and adopt a broad M_A prior of $0.75 \pm 0.15\ M_\odot$ to perform the orvara analysis (Brandt et al. 2021), again with the same MCMC setup as in Section 4. Table 5 presents our fitted and derived physical properties of Kepler-444.

With a broader M_A prior, we find that the best-fit values and credible intervals of the following parameters remain nearly unchanged compared to our results in Section 4: individual masses of B and C components (M_B, M_C), eccentricity (e), inclination (i), position angle of the ascending node (Ω), mean longitude of the primary star's orbit at epoch J2010.0 ($\lambda_{ref,\star}$), the system's parallax (ϖ) and barycentric proper motion ($\mu_\alpha\cos\delta$ and μ_δ), and the RV jitter. The resulting RV ZPs are consistent within 0.3σ, although those derived with a broader M_A prior are systematically higher by 50 m s^{-1}. In addition, the system's semimajor axis (a) and orbital period (P), the BC-to-A mass ratio, argument of the periastron of the primary star's

orbit ($\omega_\star$), the time of periastron (T_0), and the relative separation between A and BC during periastron all have consistent median values but 1.2–6× larger uncertainties with a broader M_A prior. These comparison results suggest that our orbital solution presented in Section 4 is robust even with a very broad and conservative M_A prior.

Appendix B
Orbit Analysis of Kepler-444 without Including the Observed BC−A Relative RV

Here we use orvara to constrain the barycentric orbit and dynamical mass of Kepler-444 BC by using the system's relative astrometry, absolute astrometry, and the primary star's multiepoch RVs, but excluding the observed BC−A relative RV. We set the same priors for free parameters and carry out the MCMC orbit analysis with the same number of temperatures, walkers, and steps as in Section 4. Along with the orbit fitting, we also calculate the BC−A relative RV at 2,456,783.1 JD (i.e., the mean epoch of our observed ΔRV_{BC-A}; Section 3.4) using the fitted parameters from each

chain based on the following expression:

$$
\begin{aligned}
\Delta \mathrm{RV}_{\mathrm{BC-A}} &= -\frac{2\pi \sin i \sqrt{M_{\mathrm{A}} + M_{\mathrm{BC}}}}{\sqrt{a(1 - e^2)}} \\
&\times [\cos(\nu + \omega_\star) + e\cos(\omega_\star)] \approx -4.74 \\
&\times \frac{2\pi \sin i}{\sqrt{1 - e^2}} \left(\frac{M_{\mathrm{A}} + M_{\mathrm{BC}}}{M_\odot}\right)^{1/2} \left(\frac{a}{\mathrm{au}}\right)^{-1/2} \\
&\times [\cos(\nu + \omega_\star) + e\cos(\omega_\star)]\ \mathrm{km\ s^{-1}}, \qquad (\mathrm{B1})
\end{aligned}
$$

where ν is the true anomaly. In following discussion, we use $\Delta \mathrm{RV}_{\mathrm{BC-A,ref}}$ to note this calculated single-epoch BC−A relative RV.

As shown in Figure 6, the resulting posteriors from this reanalysis are composed of two families of solutions, with one predicting positive $\Delta \mathrm{RV}_{\mathrm{BC-A,ref}}$ values (i.e., the BC component is moving away from us relative to A) and the other predicting negative $\Delta \mathrm{RV}_{\mathrm{BC-A,ref}}$ values (i.e., the BC component is moving toward us relative to A). Both families of solutions produce the same posteriors in M_{A}, which is primarily constrained by the prior, but the ones with negative $\Delta \mathrm{RV}_{\mathrm{BC-A,ref}}$ predict slightly lower masses for Kepler-444 BC. The posteriors of a, e, and i are nearly symmetric against $\Delta \mathrm{RV}_{\mathrm{BC-A,ref}} = 0$, with the eccentricity pushed toward an unphysical value of ≈ 1 when $\Delta \mathrm{RV}_{\mathrm{BC-A,ref}}$ is close to 0. In addition, the distributions of $\omega_\star$, Ω, and $\lambda_{\mathrm{ref},\star}$ are bimodal, with distinct peak-to-peak separations of $\approx 120°$, $180°$, and $180°$, respectively, suggesting that the orbits' three-dimensional orientations of these two families of solutions are completely different (Figure 7). In Table 6, we list the fitted and derived parameters and their uncertainties for each orbital solution.

We note that only 17% of the resulting MCMC chains produce negative $\Delta \mathrm{RV}_{\mathrm{BC-A,ref}}$ values, and such unequal sample sizes between two families of orbital solutions are caused because the initial MCMC parameter values are closer to those producing a positive $\Delta \mathrm{RV}_{\mathrm{BC-A,ref}}$. According to Figure 6, the computed posterior probabilities for each set of solutions are comparable. Therefore, our analysis reveals that with only the observed relative astrometry, absolute astrometry, and the primary star's RVs, we cannot distinguish between the two families of orbital solutions for the Kepler-444 system. Collecting Kepler-444 A's RVs while BC is near periapsis can help relieve the degeneracy, but this opportunity will not be available for another century (Figure 7). In contrast, even a single epoch of the observed BC−A relative RV can efficiently break this degeneracy to precisely and accurately constrain the orbital parameters (e.g., Pearce et al. 2020). Therefore, we encourage studies about the architectures of stellar binaries to consider observing the relative RV between the primary and secondary stars, especially for systems similar to Kepler-444, where the secondary is near apoapsis on a long-period orbit.
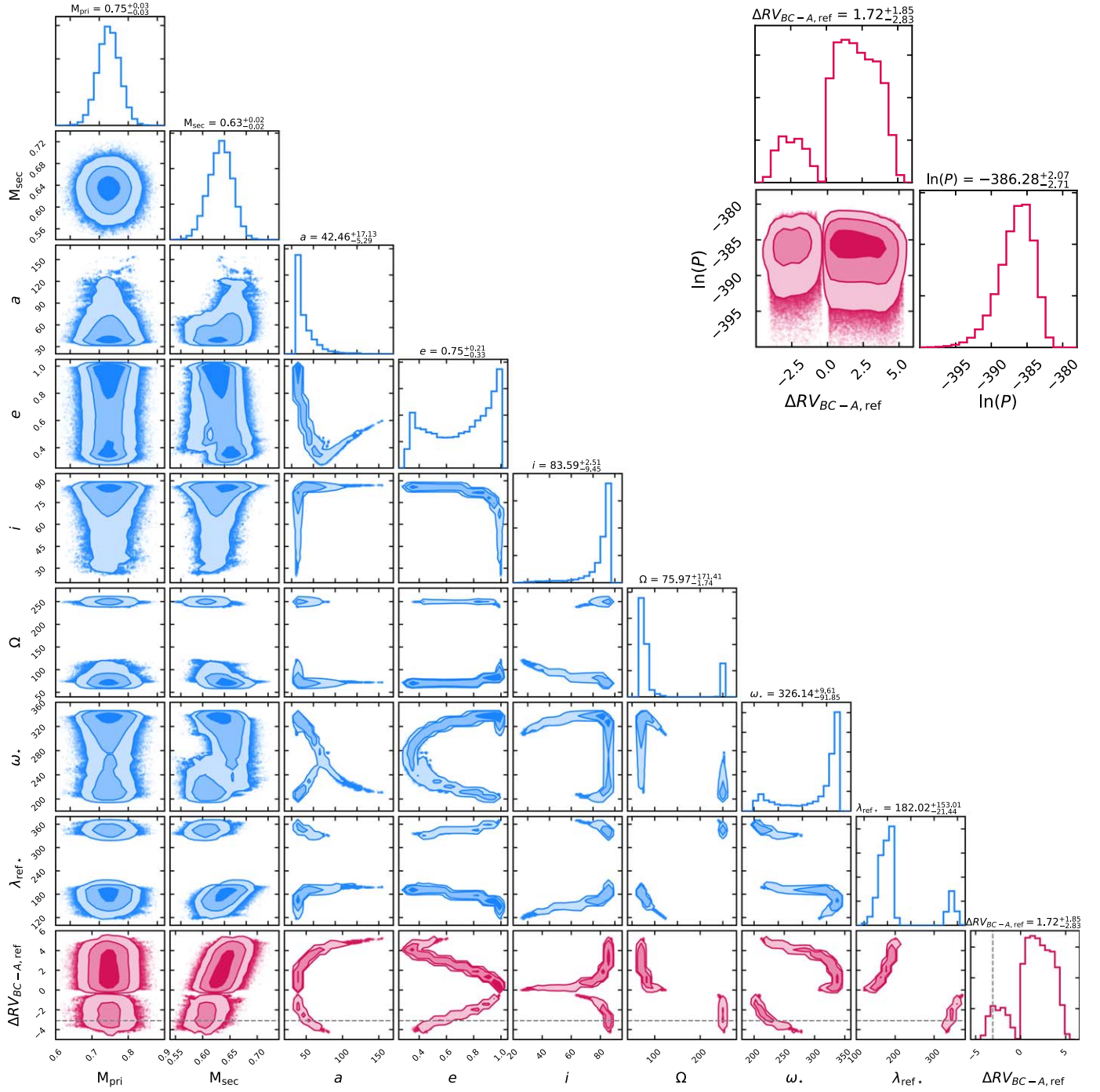
Figure 6. Posteriors of our orbit analysis of Kepler-444 without including the observed BC−A relative RV. The corresponding credible intervals and the best-fit values of these parameters are listed in Table 6. Fitted parameters are shown as the y-axis in the first eight rows of the corner plot, and the y-axis of the last row presents $\Delta RV_{BC-A,ref}$, which is the calculated BC−A relative RV at the epoch of 2,456,783.1 JD (i.e., the mean epoch of our observed ΔRV_{BC-A} value; Section 3.4). There are two families of orbital solutions, with one predicting positive $\Delta RV_{BC-A,ref}$ values and the other predicting negative $\Delta RV_{BC-A,ref}$ values. These two families of solutions have symmetric a, e, and i posteriors against $\Delta RV_{BC-A,ref} = 0$, but their Ω, $\omega_{\star}$, and $\lambda_{ref,\star}$ posteriors are bimodal, suggesting completely different three-dimensional orientations. The MCMC chains with $\Delta RV_{BC-A,ref} \approx -3.1$ km s^{-1} (horizontal dashed line) correspond to our fitted orbits in Section 4. At the top right, we show that the two families of solutions with different signs of $\Delta RV_{BC-A,ref}$ have comparable posterior probabilities, although their MCMC sample sizes are very different.
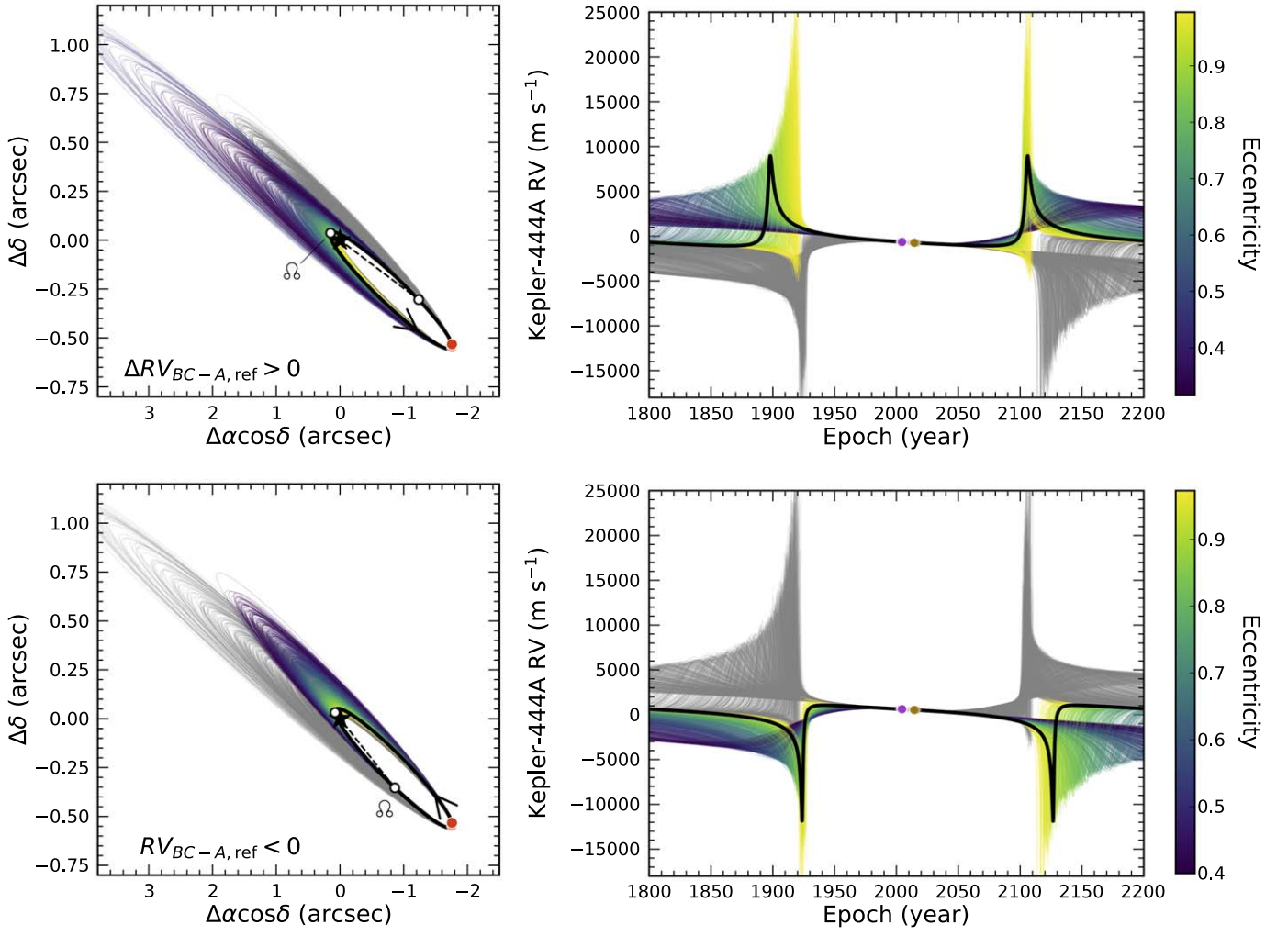
Figure 7. Top left: predicted relative astrometry between A and BC components of 1000 randomly drawn orbits from the MCMC chains with positive $\Delta RV_{BC-A,ref}$, color-coded by eccentricity. We overlay 1000 randomly drawn orbits from the MCMC chains with negative $\Delta RV_{BC-A,ref}$ and show them in gray. Similar to Figure 4, we use the black solid line to show the best-fit orbit solution with $\Delta RV_{BC-A,ref} > 0$ and use two white circles to mark the ascending (labeled) and descending nodes, connected via a dashed line. We place Kepler-444 A (black star) at ZPs and overlay the observed relative astrometry of BC (orange circles) that occupies the orbital arc at the bottom right. Top right: predicted RVs of Kepler-444 A of the randomly drawn orbits (as shown in the top left panel). Orbits with positive $\Delta RV_{BC-A,ref}$ are color-coded by eccentricities, while those with negative $\Delta RV_{BC-A,ref}$ are shown in gray, scaled to the same RV ZP. The black solid line shows predictions from the best-fit orbit, overlaid with the observed relative RVs of Kepler-444 A (purple, blue, and brown circles) color-coded by instruments in the same fashion as the bottom left panel in Figure 5. Bottom: the same format as in the top panel, but we show the orbital solution with negative $\Delta RV_{BC-A,ref}$ in colors coded by eccentricities and those with positive $\Delta RV_{BC-A,ref}$ in gray.

Table 6
Orbit Analysis of Kepler-444 without Including the Observed Relative RV between BC and A Components

Parameter[a]	Unit	Orbital Solution with Positive $\Delta RV_{BC-A,ref}$[b]			Orbital Solution with Negative $\Delta RV_{BC-A,ref}$[b]		
		Median $\pm 1\sigma$	2σ Confidence Interval	Best Fit	Median $\pm 1\sigma$	2σ Confidence Interval	Best Fit
Fitted Parameters							
Mass of Kepler-444 A, M_A	$M_\odot$	$0.75^{+0.03}_{-0.03}$	(0.69, 0.81)	0.75	$0.75^{+0.03}_{-0.03}$	(0.69, 0.81)	0.75
Mass of Kepler-444 BC, M_{BC}	$M_\odot$	$0.64^{+0.02}_{-0.02}$	(0.60, 0.67)	0.63	$0.61^{+0.02}_{-0.02}$	(0.57, 0.64)	0.61
Semimajor axis, a	au	$41.8^{+18.5}_{-4.9}$	(36.2, 94.5)	39.1	$45.1^{+11.9}_{-6.0}$	(37.3, 70.0)	38.2
$\sqrt{e}\sin\omega_\star$	...	$-0.43^{+0.04}_{-0.11}$	(−0.60, −0.36)	−0.38	$-0.48^{+0.06}_{-0.11}$	(−0.65, −0.38)	−0.41
$\sqrt{e}\cos\omega_\star$	...	$0.76^{+0.12}_{-0.48}$	(−0.37, 0.91)	0.85	$-0.69^{+0.31}_{-0.16}$	(−0.89, −0.08)	−0.87
Inclination, i	deg	$83.4^{+2.8}_{-11.4}$	(40.3, 86.9)	81.2	$84.2^{+1.6}_{-4.0}$	(73.4, 86.4)	78.0
PA of the ascending node, Ω	deg	$75.3^{+4.9}_{-1.1}$	(73.8, 101.0)	76.1	$250.2^{+0.7}_{-1.6}$	(245.6, 251.2)	247.7
Mean longitude at J2010.0, $\lambda_{ref,\star}$	deg	$177.0^{+15.4}_{-18.5}$	(138.1, 198.1)	170.3	$342.9^{+9.7}_{-7.0}$	(2.1, 358.6)	358.0
Parallax, ϖ	mas	$27.358^{+0.016}_{-0.016}$	(27.325, 27.391)	27.358	$27.358^{+0.016}_{-0.016}$	(27.325, 27.391)	27.353
System barycentric proper motion in R.A., $\mu_\alpha\cos(\delta)$	mas yr^{-1}	$94.57^{+0.03}_{-0.03}$	(94.52, 94.63)	94.57	$94.58^{+0.03}_{-0.03}$	(94.52, 94.63)	94.57
System barycentric proper motion in decl., μ_δ	mas yr^{-1}	$-631.59^{+0.04}_{-0.04}$	(−631.66, −631.51)	−631.60	$-631.61^{+0.04}_{-0.04}$	(−631.68, −631.53)	−631.59
RV jitter for HET/HRS, $\sigma_{jit,HRS}$	m s^{-1}	$5.92^{+1.58}_{-1.35}$	(3.35, 9.15)	5.81	$6.20^{+1.57}_{-1.43}$	(3.55, 9.35)	6.09
RV ZP for HET/HRS, ZP_{HRS}	m s^{-1}	-967^{+647}_{-746}	(−2154, −55)	−708	1128^{+406}_{-448}	(406, 1760)	563
RV jitter for post-upgrade HIRES, $\sigma_{jit,post-HIRES}$	m s^{-1}	$2.88^{+0.21}_{-0.19}$	(2.52, 3.31)	2.88	$2.89^{+0.19}_{-0.20}$	(2.51, 3.28)	2.78
RV ZP for post-upgrade HIRES, $ZP_{post-HIRES}$	m s^{-1}	-985^{+647}_{-746}	(−2173, −73)	−726	1110^{+406}_{-447}	(388, 1741)	545
RV jitter for pre-upgrade HIRES, $\sigma_{jit,pre-HIRES}$	m s^{-1}	$0.01^{+0.66}_{-0.01}$	(0.00, 5.03)	0.00	$0.01^{+0.62}_{-0.01}$	(0.00, 5.02)	0.12
RV ZP for pre-upgrade HIRES, $ZP_{pre-HIRES}$	m s^{-1}	-904^{+645}_{-743}	(−2088, 4)	−647	-703^{+1284}_{-868}	(−2060, 1623)	−974
Derived Parameters							
BC-to-A mass ratio, M_{BC}/M_A	...	$0.85^{+0.04}_{-0.04}$	(0.77, 0.94)	0.84	$0.81^{+0.04}_{-0.04}$	(0.74, 0.90)	0.82
Eccentricity, e	...	$0.76^{+0.20}_{-0.36}$	(0.33, 0.99)	0.86	$0.70^{+0.19}_{-0.22}$	(0.41, 0.96)	0.92
Argument of periastron, $\omega_\star$	deg	$330.5^{+5.6}_{-33.2}$	(234.2, 337.9)	335.6	$214.7^{+21.9}_{-8.4}$	(203.4, 263.2)	205.3
Period, P	yr	230^{+167}_{-38}	(185, 779)	208	259^{+110}_{-50}	(194, 502)	202
Time of periastron, T_0[c]	JD	2490955^{+5090}_{-1274}	(2483815, 2498002)	2490081	$2515913^{+36893}_{-15739}$	(2495193, 2602420)	2497876
On-sky semimajor axis, $a\times\varpi$	mas	1144^{+506}_{-133}	(990, 2584)	1068	1233^{+325}_{-164}	(1019, 1914)	1045
Minimum A−BC separation, $a(1-e)$	au	$10.0^{+27.5}_{-8.7}$	(0.2, 56.8)	5.3	$13.5^{+15.9}_{-9.1}$	(1.5, 40.9)	2.9
BC−A relative RV at 2,456,783.1 JD $\Delta RV_{BC-A,ref}$[b]	km s^{-1}	$2.2^{+1.6}_{-1.4}$	(0.2, 4.6)	1.6	$-2.5^{+1.0}_{-0.9}$	(−3.9, −0.8)	−1.2

Notes.

[a] Orbital parameters all correspond to Kepler-444 BC except for a, $\omega_\star$, and $\lambda_{ref,\star}$. The first parameter corresponds to the system's (instead of individual components') semimajor axis, and the latter two parameters correspond to those of Kepler-444 A's orbit.

[b] The $\Delta RV_{BC-A,ref}$ is computed at 2,456,783.1 JD, the mean epoch of our measured ΔRV_{BC-A} value (Section 3.4).

[c] T_0 is computed as $t_{ref} - P \times (\lambda_{ref,\star} - \omega_\star)/360°$, where $t_{ref} = 2,455,197.5$ JD (i.e., epoch J2010.0).

ORCID iDs

Zhoujian Zhang (张周健 ◉ https://orcid.org/0000-0002-3726-4881
Brendan P. Bowler ◉ https://orcid.org/0000-0003-2649-2288
Trent J. Dupuy ◉ https://orcid.org/0000-0001-9823-1445
Timothy D. Brandt ◉ https://orcid.org/0000-0003-2630-8073
G. Mirek Brandt ◉ https://orcid.org/0000-0003-0168-3010
William D. Cochran ◉ https://orcid.org/0000-0001-9662-3496
Michael Endl ◉ https://orcid.org/0000-0002-7714-6310
Kaitlin M. Kratter ◉ https://orcid.org/0000-0001-5253-1338
Howard T. Isaacson ◉ https://orcid.org/0000-0002-0531-1073
Kyle Franson ◉ https://orcid.org/0000-0003-4557-414X
Adam L. Kraus ◉ https://orcid.org/0000-0001-9811-568X
Caroline V. Morley ◉ https://orcid.org/0000-0002-4404-0456
Yifan Zhou ◉ https://orcid.org/0000-0003-2969-6040

References

Adams, F. C., Ruden, S. P., & Shu, F. H. 1989, ApJ, 347, 959
Adibekyan, V. Z., Delgado Mena, E., Sousa, S. G., et al. 2012, A&A, 547, A36
Arifyanto, M. I., & Fuchs, B. 2006, A&A, 449, 533
Artymowicz, P., & Lubow, S. H. 1994, ApJ, 421, 651
Astropy Collaboration, Price-Whelan, A. M., Sipőcz, B. M., et al. 2018, AJ, 156, 123
Astropy Collaboration, Robitaille, T. P., Tollerud, E. J., et al. 2013, A&A, 558, A33
Bailer-Jones, C. A. L., Rybizki, J., Fouesneau, M., Demleitner, M., & Andrae, R. 2021, AJ, 161, 147
Bate, M. R., Bonnell, I. A., Clarke, C. J., et al. 2000, MNRAS, 317, 773
Batygin, K. 2012, Natur, 491, 418
Behmard, A., Dai, F., & Howard, A. W. 2022, AJ, 163, 160
Bellinger, E. P., Hekker, S., Angelou, G. C., Stokholm, A., & Basu, S. 2019, A&A, 622, A130
Bensby, T., Feltzing, S., & Oey, M. S. 2014, A&A, 562, A71
Bonavita, M., Fontanive, C., Gratton, R., et al. 2022, MNRAS, 513, 5588

Bonnell, I. A., & Bate, M. R. 1994, MNRAS, 271, 999
Borkovits, T., Hajdu, T., Sztakovics, J., et al. 2016, MNRAS, 455, 4136
Bovy, J., Hogg, D. W., & Roweis, S. T. 2009, ApJ, 700, 1794
Bowler, B. P., Cochran, W. D., Endl, M., et al. 2021a, AJ, 161, 106
Bowler, B. P., Dupuy, T. J., Endl, M., et al. 2018, AJ, 155, 159
Bowler, B. P., Endl, M., Cochran, W. D., et al. 2021b, ApJL, 913, L26
Bowler, B. P., Kraus, A. L., Bryan, M. L., et al. 2017, AJ, 154, 165
Brandt, T. D. 2018, ApJS, 239, 31
Brandt, T. D. 2021, ApJS, 254, 42
Brandt, T. D., Dupuy, T. J., Li, Y., et al. 2021, AJ, 162, 186
Brewer, J. M., Fischer, D. A., Valenti, J. A., & Piskunov, N. 2016, ApJS, 225, 32
Brewer, J. M., Wang, S., Fischer, D. A., & Foreman-Mackey, D. 2018, ApJL, 867, L3
Buldgen, G., Farnir, M., Pezzotti, C., et al. 2019, A&A, 630, A126
Butler, R. P., Vogt, S. S., Laughlin, G., et al. 2017, AJ, 153, 208
Campante, T. L., Barclay, T., Swift, J. J., et al. 2015, ApJ, 799, 170
Campante, T. L., Lund, M. N., Kuszlewicz, J. S., et al. 2016, ApJ, 819, 85
Chatterjee, S., & Tan, J. C. 2014, ApJ, 780, 53
Chen, J., & Kipping, D. 2017, ApJ, 834, 17
Christian, S., Vanderburg, A., Becker, J., et al. 2022, AJ, 163, 207
Cunha, M. S., Roxburgh, I. W., Aguirre Børsen-Koch, V., et al. 2021, MNRAS, 508, 5864
Currie, T., Brandt, T. D., Kuzuhara, M., et al. 2020, ApJL, 904, L25
Czekala, I., Chiang, E., Andrews, S. M., et al. 2019, ApJ, 883, 22
Czekala, I., Ribas, Á., Cuello, N., et al. 2021, ApJ, 912, 6
Doyle, L. R., Carter, J. A., Fabrycky, D. C., et al. 2011, Sci, 333, 1602
Duchene, G., & Kraus, A. 2013, ARA&A, 51, 269
Dupuy, T. J., Kratter, K. M., Kraus, A. L., et al. 2016, ApJ, 817, 80
Dupuy, T. J., Kraus, A. L., Kratter, K. M., et al. 2022, MNRAS, 512, 648
Duquennoy, A., & Mayor, M. 1991, A&A, 248, 485
Endl, M., Kürster, M., & Els, S. 2000, A&A, 362, 585
Fischer, D. A., & Marcy, G. W. 1992, ApJ, 396, 178
Fontanive, C., Muzic, K., Bonavita, M., & Biller, B. 2019, MNRAS, 490, 1120
Foreman-Mackey, D. 2016, JOSS, 1, 24
Foreman-Mackey, D., Hogg, D. W., Lang, D., & Goodman, J. 2013, PASP, 125, 306
Fouqué, P., Moutou, C., Malo, L., et al. 2018, MNRAS, 475, 1960
Franson, K., Bowler, B. P., Brandt, T. D., et al. 2022, AJ, 163, 50
Gaia Collaboration, Brown, A. G. A., Vallenari, A., et al. 2021, A&A, 649, A1
Gaia Collaboration, Prusti, T., de Bruijne, J. H. J., et al. 2016, A&A, 595, A1
Hale, A. 1994, AJ, 107, 306
Hall, O. J., Davies, G. R., van Saders, J., et al. 2021, NatAs, 5, 707
Hatzes, A. P., Cochran, W. D., Endl, M., et al. 2003, ApJ, 599, 1383
Hayashi, C. 1981, PThPS, 70, 35
Howard, A. W., Johnson, J. A., Marcy, G. W., et al. 2010, ApJ, 721, 1467
Hunter, J. D. 2007, CSE, 9, 90
Johnson, J. A., Petigura, E. A., Fulton, B. J., et al. 2017, AJ, 154, 108
Jones, E., Oliphant, T., Peterson, P., et al. 2001, SciPy: Open Source Scientific Tools for Python, http://www.scipy.org/
Justesen, A. B., & Albrecht, S. 2020, A&A, 642, A212
Konopacky, Q. M., Marois, C., Macintosh, B. A., et al. 2016, AJ, 152, 28

Kozai, Y. 1962, AJ, 67, 591
Kratter, K., & Lodato, G. 2016, ARA&A, 54, 271
Kraus, A. L., Ireland, M. J., Huber, D., Mann, A. W., & Dupuy, T. J. 2016, AJ, 152, 8
Kuzuhara, M., Currie, T., Takarada, T., et al. 2022, ApJL, 934, L189
Lee, E. J., Chiang, E., & Ormel, C. W. 2014, ApJ, 797, 95
Li, Y., Brandt, T. D., Brandt, G. M., et al. 2021, AJ, 162, 266
Lidov, M. L. 1962, P&SS, 9, 719
Lissauer, J. J. 1987, Icar, 69, 249
Lissauer, J. J., Ragozzine, D., Fabrycky, D. C., et al. 2011, ApJS, 197, 8
Lubow, S. H., Martin, R. G., & Nixon, C. 2015, ApJ, 800, 96
Mack, C. E., Strassmeier, K. G., Ilyin, I., et al. 2018, A&A, 612, A46
Manara, C. F., Tazzari, M., Long, F., et al. 2019, A&A, 628, A95
Markwardt, C. B. 2009, in ASP Conf. Ser. 411, Astronomical Data Analysis Software and Systems XVIII, ed. D. A. Bohlender, D. Durand, & P. Dowler (San Francisco, CA: ASP), 251
Mazeh, T., Perets, H. B., McQuillan, A., & Goldstein, E. S. 2015, ApJ, 801, 3
Mills, S. M., & Fabrycky, D. C. 2017, ApJL, 838, L11
Miranda, R., & Lai, D. 2015, MNRAS, 452, 2396
Moe, M., & Kratter, K. M. 2021, MNRAS, 507, 3593
Naoz, S., Farr, W. M., Lithwick, Y., Rasio, F. A., & Teyssandier, J. 2013, MNRAS, 431, 2155
Offner, S. S. R., Moe, M., Kratter, K. M., et al. 2022, arXiv:2203.10066
Oliphant, T. 2006, NumPy: A Guide to NumPy (USA: Trelgol Publishing), http://www.numpy.org/
Pearce, L. A., Kraus, A. L., Dupuy, T. J., et al. 2020, ApJ, 894, 115
Perez, F., & Granger, B. E. 2007, CSE, 9, 21
Rafikov, R. R., & Silsbee, K. 2015, ApJ, 798, 69
Raghavan, D., McAlister, H. A., Henry, T. J., et al. 2010, ApJS, 190, 1
Ricker, G. R., Winn, J. N., Vanderspek, R., et al. 2015, JATIS, 1, 014003
Service, M., Lu, J. R., Campbell, R., et al. 2016, PASP, 128, 095004
Shetrone, M., Cornell, M., Fowler, J., et al. 2007, PASP, 119, 556
Sigalotti, L. D. G., Cruz, F., Gabbasov, R., Klapp, J., & Ramirez-Velasquez, J. 2018, ApJ, 857, 40
Silsbee, K., & Rafikov, R. R. 2015, ApJ, 798, 71
Silva Aguirre, V., Davies, G. R., Basu, S., et al. 2015, MNRAS, 452, 2127
Sozzetti, A., Torres, G., Latham, D. W., et al. 2009, ApJ, 697, 544
Tayar, J., Claytor, Z. R., Huber, D., & van Saders, J. 2022, ApJ, 927, 31
Thébault, P., Marzari, F., & Scholl, H. 2006, Icar, 183, 193
Tobin, J. J., Kratter, K. M., Persson, M. V., et al. 2016, Natur, 538, 483
Tokovinin, A. 2018, AJ, 155, 160
Tull, R. G. 1998, Proc. SPIE, 3355, 387
Vousden, W. D., Farr, W. M., & Mandel, I. 2016, MNRAS, 455, 1919
Wang, J., Xie, J. -W., Barclay, T., & Fischer, D. A. 2014, ApJ, 783, 4
Weidenschilling, S. J. 1977, Ap&SS, 51, 153
Wilson, O. C. 1941, ApJ, 93, 29
Wizinowich, P. 2013, PASP, 125, 798
Yelda, S., Lu, J. R., Ghez, A. M., et al. 2010, ApJ, 725, 331
Zanazzi, J. J., & Lai, D. 2018, MNRAS, 477, 5207
Zeng, Y., Brandt, T. D., Li, G., et al. 2022, AJ, 164, 188
Ziegler, C., Tokovinin, A., Latiolais, M., et al. 2021, AJ, 162, 192